

AMATH 575 Group Project: Turing Instability

Yuan Gao, Zihuan Zhang, Tailai Li, Runfeng Xue

June 25, 2025

1 Introduction

Pattern formation in chemical and biological systems is often modeled using reaction–diffusion equations. A landmark concept introduced by Alan Turing in 1952 (Turing, 1952) demonstrated that chemical reactions coupled with diffusion can spontaneously generate spatial patterns from an initially homogeneous state. This pattern, known as the Turing pattern, emerges from a diffusion-driven instability, where the combination of reaction kinetics and differing diffusion rates disrupts a uniform state and leads to the formation of organized structures such as stripes or spots. Notably, this mechanism was surprising because diffusion alone was expected to homogenize concentrations, but in the presence of suitable reaction dynamics it leads to self-organized patterning. Turing’s insight is deeply impactful, offering a theoretical framework to explain how complex patterns naturally arise, from animal skin patterns to the spatial distribution of morphogens during embryo development. Indeed, reaction–diffusion systems have become central in pattern formation research as prototype models, capable of producing fronts, hexagons, spirals, stripes and other spatial motifs in their solutions.

Among reaction–diffusion models, the Gray-Scott model has played an important role in the study of Turing-like pattern formation. The Gray-Scott model is a two-species autocatalytic reaction–diffusion system (Gray & Scott, 1984) that exhibits a remarkable diversity of spatiotemporal patterns under different parameter settings. By tuning its feed rate and removal rate, this model can produce classic stationary Turing patterns (such as stable spots and stripes) as well as exotic behaviors including oscillatory labyrinths, moving fronts, and self-replicating spot patterns. Numerical studies have revealed that even this relatively simple model generates an unprecedented range of patterns – from regular hexagonal spot arrays to irregular stationary distributions and even chaotic, time-dependent structures. These findings, beginning with Pearson’s seminal numerical experiments (Pearson, 1993), established the Gray-Scott model as a canonical example for exploring pattern-formation mechanisms. It is a useful model for testing ideas because its complex behavior is similar to what we see in real chemical and biological systems.

To understand how these patterns form, researchers often use both numerical simulations and lin-

ear stability analysis. Linear stability analysis, also known as Turing analysis, studies reaction–diffusion equations near a steady state to find out when spatial disturbances make the system unstable. This method gives the conditions for Turing instability, such as inequalities between reaction rates and diffusion rates. It also predicts the typical wavelength of the pattern that will form. In practice, the analysis tells us which parameter values will cause small random disturbances to grow into repeating spatial patterns. To study more than the first stage, researchers use full numerical simulations of the nonlinear Gray-Scott model to see how patterns develop and change over time. Simulations support the theory by showing when patterns begin to form. They also show how patterns grow, change over time, and interact, such as splitting, merging, or competing. By combining theory and simulation, we can better understand how these patterns actually form and behave.

We computed how the range of the stability of fixed point B_e^\pm changes in the Gray-Scott model when the relative strength of the reaction terms τ varied. We found that the original calculation of the upper and lower bounds of τ in the paper was incorrect, and we provided corrected bounds. As an extension, we examined the patterns that emerge when the stability of B_e^\pm changes. Specifically, we refer to the patterns that arise when B_e^\pm transitions from stable to unstable as *classic Turing patterns*, and those that emerge when B_e^\pm transitions from one unstable state to another as *extended Turing patterns*.

2 Description of Model

2.1 Turing Pattern and Turing Instability

Alan M. Turing proposed the idea of the Turing pattern in his paper *The Chemical Basis of Morphogenesis* (Turing, 1952). He suggested that the interaction between two diffusing chemical species, which now commonly referred to as morphogens, can lead to the spontaneous formation of spatial patterns. In the context of reaction-diffusion systems, these spatial patterns can be understood as special types of steady states of the system. However, the concept of a fixed point in such systems differs from that in ordinary differential equations (ODEs). In an ODE system, a fixed point typically refers to a constant solution in time, representing a point in phase space. But in reaction-diffusion systems, due to the spatial dependence, a fixed point corresponds to a steady-state spatial distribution. i.e. a solution that is constant in time but varies in space.

For instance, in the Gray–Scott model without diffusion, the fixed point is simply a uniform concentration which is a zero-dimensional object. When diffusion is introduced, the system can instead converge to a non-uniform, two-dimensional structure like a spatially varying steady state. Mathematically, this is interpreted as a fixed point in an infinite-dimensional function space.

Understanding this reinterpretation of fixed points lays the foundation for Classical Turing instability. A Turing pattern arises when a uniform steady state is stable in the absence of spatial variation

(i.e., under homogeneous perturbations) but becomes unstable when small spatial perturbations are introduced. This means the system resists temporal disturbances and maintains equilibrium over time, yet is sensitive to certain spatial modes that can grow and form patterns.

If the steady state is stable under both temporal and spatial perturbations, then the system remains in the uniform state and no pattern emerges. On the other hand, if the steady state is unstable under all perturbations, it will never be reached and the system may become chaotic or diverge. Therefore, the necessary condition for pattern formation is a balance: the steady state must be temporally stable but spatially unstable within a certain band of wave numbers. This band determines which spatial frequencies (or scales) can grow to form patterns. Once the perturbations amplify and stabilize, the system settles into a new non-uniform steady state—this is the observable Turing pattern.

2.2 Gray Scott Model

The Gray Scott Model is a modified version of the Selkov model, which describes how glycolysis works with self-catalysis developed by Gray and Scott.

The Gray-Scott model explains how a simple self-catalyzing reaction works in a still, evenly mixed flow reactor. The reactor is placed in a narrow space between two walls. Substance A comes from a tank where its density is fixed at A_0 , and flows into the reactor through the walls at rate k_f . Inside, it reacts with intermediate B in an autocatalytic reaction at rate k_1 . Then B turns into product C at rate k_2 . Finally, C , along with unused A and B , leaves the reactor at the same rate k_f .



To describe the reactions above, we use this ODE system to represent the chemical dynamic system.

$$\frac{\partial A}{\partial t} = k_f(A_0 - A) - k_1 B^2 A + D_A \nabla^2 A, \quad (3)$$

$$\frac{\partial B}{\partial t} = -(k_f + k_2)B + k_1 B^2 A + D_B \nabla^2 B. \quad (4)$$

where D_A and D_B are the diffusion coefficients of species A and B , $D_A > 0$, $D_B > 0$. To control the time scale and length scale, non-dimensionalization can be introduced

$$\tau_A = \frac{1}{k_f}, \quad \tau_B = \frac{1}{k_f + k_2}, \quad l_A = (D_A \tau_A)^{1/2}, \quad l_B = (D_B \tau_B)^{1/2}. \quad (5)$$

$$\tilde{A} = \frac{A}{A_0}, \quad \tilde{B} = \frac{B}{B_0}, \quad V_0 = \left(\frac{k_f}{k_1} \right)^{1/2}. \quad (6)$$

where $D_A = \frac{\tau_A^{\text{LBM}-0.5}}{3}$, $D_B = \frac{\tau_B^{\text{LBM}-0.5}}{3}$ are LBM relaxation parameters. LBM relaxation parameters control how quickly the particle distribution returns to its equilibrium. Now insert these variables in the ODE system

$$\tau_A \frac{\partial \tilde{A}}{\partial t} = -\tilde{B}^2 \tilde{A} + 1 - \tilde{A} + l_A^2 \nabla^2 \tilde{A}, \quad (7)$$

$$\tau_B \frac{\partial \tilde{B}}{\partial t} = +\eta \tilde{B}^2 \tilde{A} - \tilde{B} + l_B^2 \nabla^2 \tilde{B}. \quad (8)$$

where $\eta = U_0 (k_1 k_f)^{1/2} / (k_f + k_2)$ is the strength of the activation process, $\eta > 0$, then rescale the time and length scale by dividing τ_U and l_U , respectively.

$$\frac{\partial A}{\partial t} = -B^2 A + 1 - A + \nabla^2 A$$

$$\frac{1}{\tau} \frac{\partial B}{\partial t} = \eta B^2 A - B + \frac{1}{\epsilon^2} \nabla^2 B$$

We note $A = \tilde{A}$, $B = \tilde{B}$ and $\tau = \frac{\tau_A}{\tau_B}$, $\epsilon = \frac{l_A}{l_B} = \sqrt{\frac{\tau_A D_A}{\tau_B D_B}}$. τ indicates relative strength of the reaction terms. Meanwhile, we suppose $\tau > 0.5$. Based on this ODE system, we can analyze its property.

3 Math Derivation

Consider Eq. (25) and (26) from the paper (Ayodele et al., 2011). For simplicity and clarity of notation, let $A := \tilde{A}$, $B := \tilde{B}$, $t := \tilde{t}$. Then, we obtain the following rescaled system:

$$\frac{\partial A}{\partial t} = -B^2 A + 1 - A + \nabla^2 A \quad (9)$$

$$\frac{1}{\tau} \frac{\partial B}{\partial t} = \eta B^2 A - B + \frac{1}{\epsilon^2} \nabla^2 B \quad (10)$$

3.1 Fixed Points

At equilibrium, space is homogeneous (i.e., $\nabla^2 = 0$). Setting the time derivatives to zero, equations (9) and (10) reduce to:

$$-B^2 A + 1 - A = 0 \quad (11)$$

$$\eta B^2 A - B = 0 \quad (12)$$

From Eq. (12), we factor:

$$B(\eta B A - 1) = 0$$

This yields two possibilities: $B = 0 \Rightarrow A = 1$, or $\eta B A = 1 \Rightarrow$

$$B = \frac{1}{\eta A} \quad (13)$$

Substituting $B = \frac{1}{\eta A}$ into Eq. (11):

$$-\left(\frac{1}{\eta A}\right)^2 A + 1 - A = 0 \quad \Rightarrow \quad \eta^2 A^2 - \eta^2 A + 1 = 0$$

Solving the quadratic equation gives the fixed points:

$$\text{f.p. 1: } x_1^* = (A_e, B_e) = (1, 0)$$

$$\text{f.p. 2: } x_2^* = (A_e^+, B_e^+) = \left(\frac{\eta + \sqrt{\eta^2 - 4}}{2\eta}, \frac{\eta - \sqrt{\eta^2 - 4}}{2} \right)$$

$$\text{f.p. 3: } x_3^* = (A_e^-, B_e^-) = \left(\frac{\eta - \sqrt{\eta^2 - 4}}{2\eta}, \frac{\eta + \sqrt{\eta^2 - 4}}{2} \right)$$

Also note that:

$$\begin{aligned} B_e^\pm + \frac{1}{B_e^\pm} &= \frac{\eta \mp \sqrt{\eta^2 - 4}}{2} + \frac{2}{\eta \mp \sqrt{\eta^2 - 4}} \\ &= \frac{\eta \mp \sqrt{\eta^2 - 4} + \eta \pm \sqrt{\eta^2 - 4}}{2} \\ &= \frac{\eta + \eta}{2} \\ &= \eta. \end{aligned}$$

Thus, we obtain the equation:

$$\eta B_e^\pm = (B_e^\pm)^2 + 1 \quad (14)$$

Note that Eqs. (13) and (14) only hold for f.p. 2 and 3.

3.2 Linearization Subject to Perturbation

One key assumption made by the author is that the system is **isotropic**, meaning it exhibits identical behavior in both the x - and y -directions. As a result, it is sufficient to consider spatial perturbations along a single spatial dimension—specifically, the x -direction. Thus, we reduce our analysis to a one-dimensional form and express perturbations as:

$$P = \phi e^{\alpha t + i q x},$$

where ϕ denotes the amplitude, α the growth rate, and q the wave number of the perturbation.

3.2.1 Spatially Homogeneous Perturbation

Now, consider small perturbations around the steady state (A_e, B_e) of the form:

$$A(x, t) = A_e + \phi_A e^{\alpha t}, \quad B(x, t) = B_e + \phi_B e^{\alpha t}.$$

Substituting it into Eqs. (9)–(10) and linearizing (i.e., ignoring higher-order terms in t and x), we obtain a linear system as follows. For detail computation, please check Appendix 7.2:

$$\alpha \begin{pmatrix} \phi_B \\ \phi_A \end{pmatrix} = M(0) \begin{pmatrix} \phi_B \\ \phi_A \end{pmatrix},$$

where $M(0)$ is the Jacobian matrix at $q=0$:

$$M(0) = \begin{pmatrix} \tau(2\eta A_e B_e - 1) & \tau\eta B_e^2 \\ -2A_e B_e & -(B_e^2 + 1) \end{pmatrix} \quad (15)$$

3.2.2 Spatially Inhomogeneous Perturbation

For spatially inhomogeneous perturbations, we add an extra space perturbation along x as follows.

$$A(x, t) = A_e + \phi_A e^{\alpha t + i q x}, \quad B(x, t) = B_e + \phi_B e^{\alpha t + i q x}.$$

Using a similar procedure as in the previous case, we have:

$$\alpha \begin{pmatrix} \phi_B \\ \phi_A \end{pmatrix} = M(q^2) \begin{pmatrix} \phi_B \\ \phi_A \end{pmatrix},$$

where

$$M(q^2) = \begin{pmatrix} \tau \left(2\eta A_e B_e - 1 - \frac{q^2}{\epsilon^2} \right) & \tau \eta B_e^2 \\ -2A_e B_e & -(q^2 + B_e^2 + 1) \end{pmatrix} \quad (16)$$

3.3 Stability of the Steady State (Fixed Point)

3.3.1 Turing Instability in Terms of the Determinant and Trace of the Matrix $M(q^2)$

To analyze the conditions under which a Turing instability occurs, we examine the eigenvalues of the matrix $M(q^2)$, which governs the linearized dynamics of small perturbations around the steady state. The eigenvalues α satisfy the characteristic equation:

$$\alpha^2 - \alpha \operatorname{tr}(M(q^2)) + \det(M(q^2)) = 0,$$

which yields:

$$\alpha_{1,2} = \frac{1}{2} \left(\operatorname{tr}(M(q^2)) \pm \sqrt{\operatorname{tr}(M(q^2))^2 - 4 \det(M(q^2))} \right).$$

Here, both the trace and determinant are functions of the wave number squared, q^2 . To characterize the conditions under which Turing instability occurs, we refer to Figure 1.

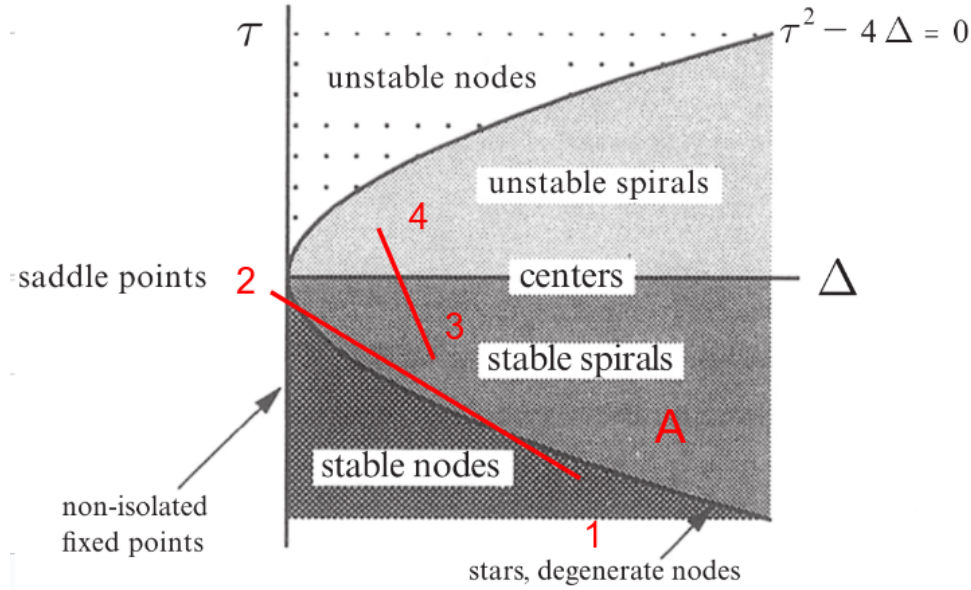


Figure 1: Figure 5.2.8 from Strogatz's book *Nonlinear Dynamics and Chaos*, illustrating the behavior of the trace and determinant of $M(q^2)$ and the onset of Turing instability. (Strogatz, 2015)

A Turing instability (Classic) occurs when the steady state is stable to homogeneous perturbations (i.e., when $q = 0$) but becomes unstable to inhomogeneous perturbations (i.e., for some $q > 0$). This defines the condition under which a Turing pattern can emerge.

The first requirement is that the steady state must be stable to homogeneous perturbations. In

other words, the fixed point must lie in region A, the fourth quadrant of Figure 1. Therefore, the following conditions must be satisfied:

$$\begin{cases} \text{tr}(M(0)) < 0 \\ \det(M(0)) > 0 \end{cases} \quad (17)$$

The second requirement is that the steady state becomes unstable to inhomogeneous perturbations for some $q > 0$. There are two typical pathways, leading to two different types of bifurcations.

Case 1: Saddle Node Bifurcation If the determinant of the fixed point is decreasing for some $q > 0$, then the route to instability is via a saddle-point bifurcation. Suppose the fixed point has its determinant and trace corresponding to point 1 in Figure 1. Then the transition follows the path from 1 to 2. For this to occur, the determinant must become negative while the other condition still holds:

$$\begin{cases} \text{tr}(M(0)) < 0 \\ \det(M(0)) > 0 \end{cases} \implies \begin{cases} \text{tr}(M(q^2)) < 0 \\ \det(M(q^2)) < 0 \text{ for some } q > 0 \end{cases} \quad (18)$$

Case 2: Hopf bifurcation If the trace, on the other hand, of the fixed point is increasing for some $q > 0$, then the route to instability is via a Hopf bifurcation. Suppose the fixed point has its determinant and trace corresponding to point 3 in Figure 1. Then the transition follows the path from 3 to 4. This occurs when the trace becomes positive for some $q > 0$, while the determinant remains positive:

$$\begin{cases} \text{tr}(M(0)) < 0 \\ \det(M(0)) > 0 \end{cases} \implies \begin{cases} \text{tr}(M(q^2)) > 0 \text{ for some } q > 0 \\ \det(M(q^2)) > 0 \end{cases} \quad (19)$$

3.3.2 Fixed Point $x_1^* = (A_e, B_e) = (1, 0)$

At x_1^* , we have the following by substituting $(A_e, B_e) = (1, 0)$ into (16) and (15):

$$M(0) = M(q^2) = \begin{pmatrix} -\tau & 0 \\ 0 & -1 \end{pmatrix}$$

Hence, we have the eigenvalues (as $\tau > 1$):

$$\alpha_1 = -\tau \quad \alpha_2 = -1$$

Since both eigenvalues are negative, this fixed point is stable in both the spatially homogeneous and spatially inhomogeneous states. This means that even with the existence of a perturbation, the system will not change its spatial structure. Hence, no Turing pattern will appear in this case.

3.3.3 Fixed Point x_2^*, x_3^*

Using the identities in Eqs. (13) and (14), we can further simplify the Jacobian matrix to:

$$M(q^2) = \begin{pmatrix} \tau - \frac{\tau q^2}{\epsilon^2} & \tau\eta(\eta B_e^\pm - 1) \\ -\frac{2}{\eta} & -(q^2 + \eta B_e^\pm) \end{pmatrix} \quad (20)$$

$$M(0) = \begin{pmatrix} \tau & \tau\eta(\eta B_e^\pm - 1) \\ -\frac{2}{\eta} & -\eta B_e^\pm \end{pmatrix} \quad (21)$$

For the **homogeneous case**:

$$\text{tr}(M(0)) = \tau - \eta B_e^\pm \quad (22)$$

and

$$\det(M(0)) = \tau(\eta B_e^\pm - 2) \quad (23)$$

For the **inhomogeneous case**:

$$\text{tr}(M(q^2)) = \tau - \eta B_e^\pm - q^2 \left(\frac{\tau}{\epsilon^2} + 1 \right) \quad (24)$$

and

$$\det(M(q^2)) = \tau(q^4 \frac{1}{\epsilon^2} + q^2 \left(\frac{\eta B_e^\pm}{\epsilon^2} - 1 \right) + (\eta B_e^\pm - 2)) \quad (25)$$

To ensure the existence of these two fixed points, we consider the case of $\eta > 2$. Therefore, we know:

$$(\eta B_e^+ - 2) < 0 \quad \text{and} \quad (\eta B_e^- - 2) > 0. \quad (26)$$

For the state B_e^+ , $\text{Det}(M)(0) < 0$ and $\text{Det}(M)(q^2) < 0$ for some $q^2 > 0$. Regardless of the sign of $\text{Tr}(M)$, the eigenvalues have one positive and one negative in both the homogeneous and inhomogeneous states. (A_e^+, B_e^+) is always unstable.

For the state B_e^- in homogeneous state, both solutions $\alpha_{1,2}$ will have the same sign as $\text{Tr}(M)$ and thus the state B_e^- is stable provided $\text{Tr}(M) < 0$. That is,

$$\tau < \eta B_e^-. \quad (27)$$

For the state B_e^- in inhomogeneous state, if $\text{Det}(M)(q^2) < 0$ for some $q^2 > 0$, B_e^- is unstable by the specific perturbation. In this case, a specific perturbation changes the instability of B_e^- and a

Turing pattern may occur. We want to explore the range of parameters that may produce this Turing instability. From Eqs. (25), $|M(q^2)|$ is a parabola in q^2 which attains its minimum value for

$$q^2 = \frac{\epsilon^2 - \eta B_e^-}{2}. \quad (28)$$

Since $q^2 > 0$, a minimum in $|M(q^2)|$ exists only if $\epsilon^2 > \eta B_e^-$.

We also need another condition that the discriminant is greater than 0. Then we obtain

$$\epsilon^2 < 3\eta B_e^- - 4 - \sqrt{8\eta B_e^{-2} - 24\eta B_e^- + 16} \quad (29)$$

or

$$\epsilon^2 > 3\eta B_e^- - 4 + \sqrt{8\eta B_e^{-2} - 24\eta B_e^- + 16} \quad (30)$$

For the case $\eta > 2$, we always have

$$3\eta B_e^- - 4 - \sqrt{8\eta B_e^{-2} - 24\eta B_e^- + 16} < \eta B_e^- < 3\eta B_e^- - 4 + \sqrt{8\eta B_e^{-2} - 24\eta B_e^- + 16}. \quad (31)$$

Therefore, when

$$\epsilon^2 > 3\eta B_e^- - 4 + \sqrt{8\eta B_e^{-2} - 24\eta B_e^- + 16}, \quad (32)$$

the state B_e^- becomes unstable in homogeneous state. From the relationship of parameters τ and ϵ , $\tau = \frac{D_B}{D_A} \epsilon^2$. We require

$$\frac{D_B}{D_A} (3\eta B_e^- - 4 + \sqrt{8\eta B_e^{-2} - 24\eta B_e^- + 16}) < \tau < \eta B_e^- \quad (33)$$

The lower bound ensures that B_e^- is unstable in the inhomogeneous case, and the upper bound ensures that B_e^- is stable in the homogeneous case.

4 Simulation and Discussion

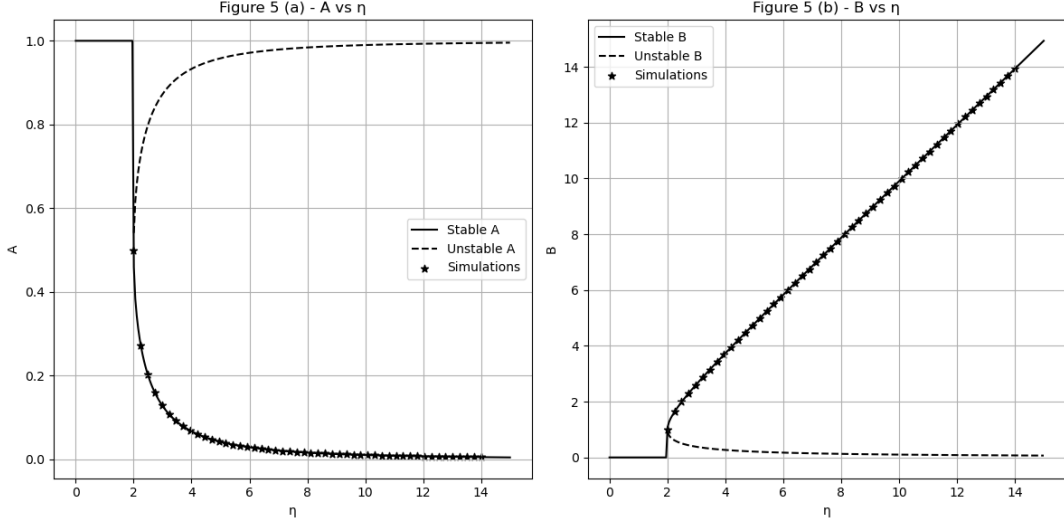


Figure 2: Bifurcation diagram of the Gray-Scott model. (a) Steady-state concentration A versus activation parameter η . (b) Steady-state concentration B versus activation parameter η .

Figure 2 shows the dependence of steady-state concentrations of A and B on the activation parameter η . The diagrams compare theoretical solutions with lattice Boltzmann simulation results.

(a) Steady-state values of A versus η : the solid line represents the stable branch A_e^- , and the dashed line represents the unstable branch A_e^+ .

(b) Steady-state values of B versus η : the solid line shows the stable branch B_e^- , and the dashed line shows the unstable branch B_e^+ .

In both panels, the black stars indicate simulation results from the lattice Boltzmann method, which closely follow the theoretical predictions.

Notice that a saddle-node bifurcation occurs at $\eta = 2$, beyond which two nontrivial steady states coexist with the trivial solution $(A_e, B_e) = (1, 0)$.

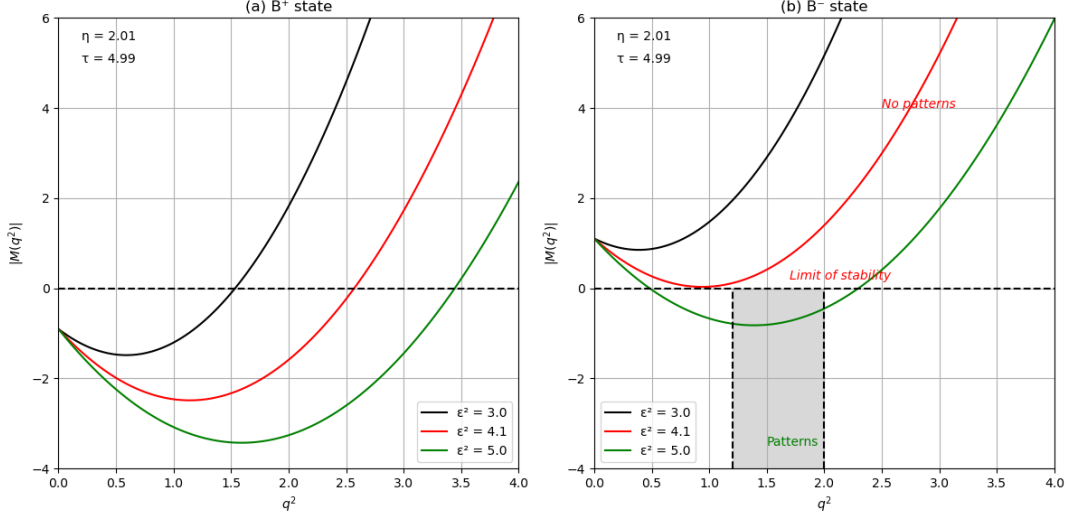


Figure 3: (a) The determinant of the Jacobian matrix versus the wave number q^2 for B^+ . (b) The determinant of the Jacobian matrix versus the wave number q^2 for B^- .

Figure 3 is the stability analysis of the Gray-Scott model in terms of the dispersion relation $\text{tr}(M(q^2))$ for different values of the diffusion parameter ϵ^2 , with fixed parameters $\eta = 2.01$, $\tau = 4.99$, and $k = 3$. The horizontal axis represents q^2 , and the vertical axis shows the real part of the eigenvalue magnitude $|\text{tr}(M(q^2))|$. Negative values indicate instability and potential for pattern formation.

(a) For the B^+ steady state. For all tested values of the diffusion ratio $\epsilon^2 = 3.0, 4.1$, and 5.0 , the function remains negative at $q = 0$, indicating that the B_e^+ state is always unstable and may lead to pattern formation. However, this state is physically unstable and cannot persist in the long term.

(b) For the B^- steady state, different regimes emerge depending on ϵ^2 . For the stable steady state (A_e^-, B_e^-) , pattern formation is only possible when ϵ^2 lies within a specific range. The shaded region highlights the instability band for $\epsilon^2 = 5.0$, where $|M(q^2)| < 0$ holds over a finite range of q^2 , indicating Turing instability. In contrast, for $\epsilon^2 = 4.1$ the system is at the stability threshold, and for $\epsilon^2 = 3.0$ the system remains stable for all perturbations.

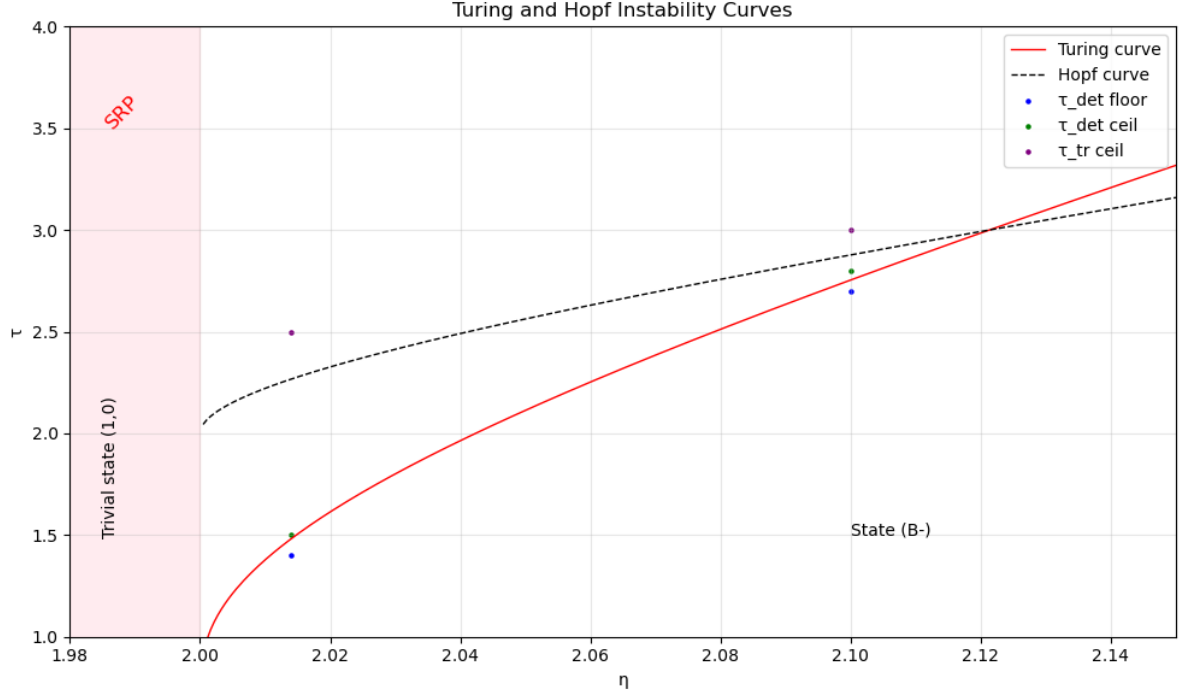


Figure 4: The parameter space in terms of the activation strength η and timescale ratio τ

Figure 4 illustrates the bifurcation diagram in the parameter space defined by the activation strength η and the timescale ratio τ for the state (A_e^-, B_e^-) .

The solid red curve indicates the onset of Turing instability, where the homogeneous steady state loses stability to spatially periodic perturbations, leading to stationary Turing patterns. The dashed black curve marks the Hopf bifurcation boundary, beyond which temporal oscillations emerge due to a pair of complex conjugate eigenvalues crossing the imaginary axis.

The shaded pink region on the left corresponds to the trivial steady state $(A_e, B_e) = (1, 0)$, which is linearly stable. However, sufficiently large perturbations in this region can induce self-replicating spot (SRP) dynamics, highlighting nonlinear pattern formation beyond linear theory.

The region between the Turing and Hopf curves is referred to as the Turing space, where classical stationary patterns are expected to emerge.

To validate our theoretical predictions, we selected two values of η and, for each, tested three τ values: one below the Turing curve (blue dots), one within the Turing space (green dots), and one above the Hopf curve (purple dots). The resulting simulations confirm that classical Turing patterns predominantly occur within the predicted instability region.

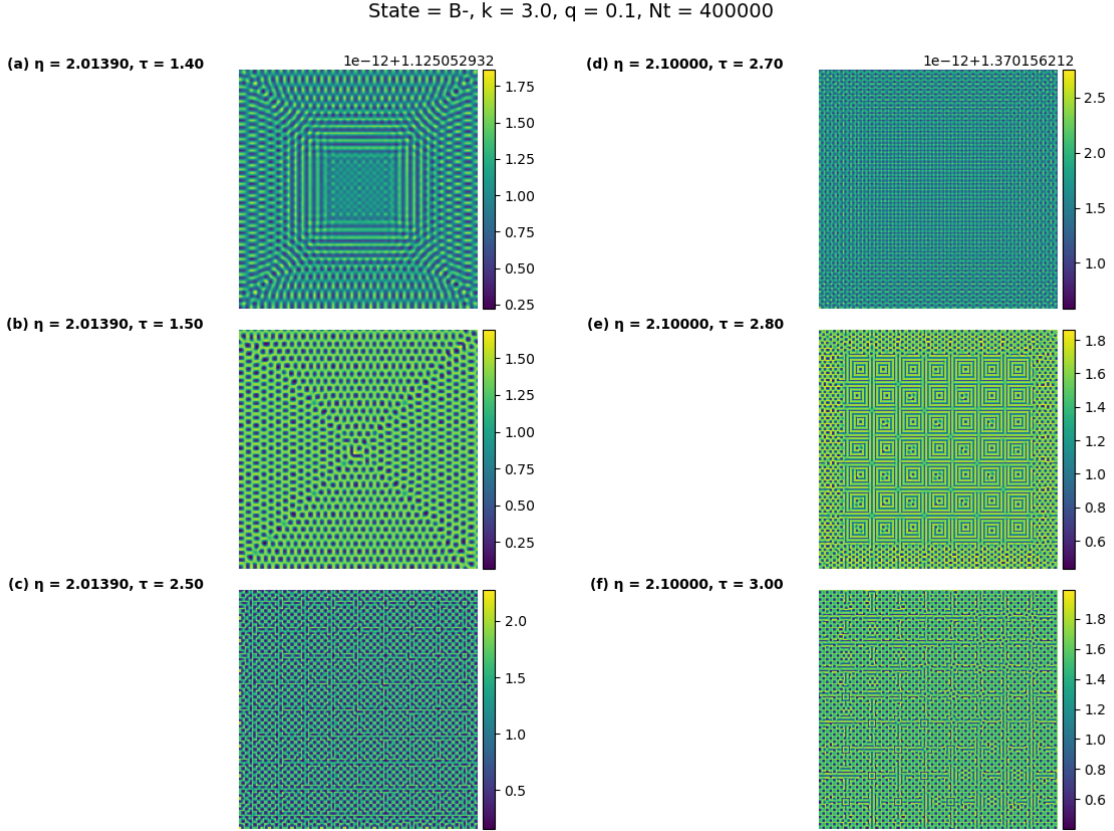


Figure 5: Simulated spatial patterns of species B in the Gray-Scott model at selected (η, τ) values

Figure 5 shows the simulation results validating the theoretical bifurcation diagram in the (η, τ) parameter space for the (A_e^-, B_e^-) steady state of the Gray-Scott model. The selected points correspond to different regions relative to the Turing and Hopf bifurcation boundaries predicted by linear stability analysis.

(a–c): For $\eta = 2.0139$, the values of $\tau = 1.40$, 1.50 , and 2.50 correspond to locations below the Turing curve, within the Turing space, and above the Hopf curve, respectively. These plots exhibit a progression from no clear pattern to classical Turing hexagons, and then to dense lattice structures beyond the classical instability region.

(d–f): For $\eta = 2.1000$, we test $\tau = 2.70$, 2.80 , and 3.00 . Clear square-like patterns emerge within the Turing space at $\tau = 2.80$, while deformed or suppressed structures are seen outside (at $\tau = 2.70$ and 3.00). Interestingly, we also observe Turing-like patterns even above the Hopf boundary.

These unexpected results suggest the presence of extended Turing patterns—stationary spatial structures that emerge outside the classically predicted instability region. This phenomenon points to nonlinear mechanisms beyond linear stability theory, opening a new direction for investigating the

conditions and mechanisms behind these extended patterns.

5 Extension and Contribution

Our work extends the classical linear stability analysis of the Gray-Scott reaction-diffusion model by incorporating both theoretical bifurcation boundaries and nonlinear simulation results. We constructed a bifurcation diagram in the (η, τ) parameter space, identifying the onset of Turing instability (solid red curve) and the Hopf bifurcation boundary (dashed black curve). Traditionally, stationary spatial patterns are expected to arise only in the region bounded between these two curves, referred to as the *Turing space*.

However, through detailed Lattice Boltzmann simulations, we discovered a previously overlooked phenomenon: spatially periodic patterns can still emerge above the Hopf boundary, where linear theory predicts only temporal oscillations. We term these patterns *extended Turing patterns*, which suggest the influence of nonlinear dynamics and subcritical mechanisms beyond the scope of eigenvalue-based analysis.

Additionally, we confirmed that the trivial state $(A_e, B_e) = (1, 0)$ remains linearly stable in the low- η regime, yet can give rise to self-replicating spot (SRP) dynamics under finite-amplitude perturbations, highlighting the limitations of linear stability predictions.

Most importantly, during our theoretical analysis, we identified and corrected a key error in the original paper concerning the derivation of the Turing instability condition. Specifically, we revised the analytical expressions for the determinant and trace of the Jacobian matrix and recalculated the Turing instability boundary accordingly. Our corrected version yields results that align much more closely with simulation data.

6 Conclusion

In this study, we explore how changing τ affects Turing pattern formation, system stability, and how spatial patterns develop in the Gray-Scott model. Using linear stability analysis, we find out how the conditions for pattern formation change when the activation strength η and diffusion ratio τ vary, and through numerical simulations we examine the resulting pattern configurations and their time evolution as τ is varied. The goal is to understand how the diffusion ratio affects the Gray-Scott system specifically, how changing τ influences pattern type, stability, and wavelength. By combining stability analysis and simulations for different τ values, we show that the original range of τ used in past work was incorrect (Ayodele et al., 2011), and we provide a corrected range. This gives a better understanding of how the diffusion ratio affects the formation and stability of Turing patterns in the Gray-Scott model.

7 Appendix

7.1 Code

All of our code, including the simulation and replication of figures from articles, are in the GitHub repository at https://github.com/ivanygao/UW_AMATH575_Turning_Instability.git.

7.2 Calculation of Jacobian Matrix

We consider the reaction-diffusion system:

$$\frac{\partial A}{\partial t} = -B^2 A + 1 - A + \nabla^2 A$$

$$\frac{1}{\tau} \frac{\partial B}{\partial t} = \eta B^2 A - B + \frac{1}{\epsilon^2} \nabla^2 B$$

Assuming isotropy, we have the perturbation around equilibrium as:

$$A = A_e + \phi_A e^{\alpha t + i k x}, \quad B = B_e + \phi_B e^{\alpha t + i k x}$$

Now plug it into the original equations and linearize to first order in ϕ .

From the first equation, Equation (9) \implies :

$$\begin{aligned} \alpha \phi_A e^{\alpha t + i k x} &= - (B_e + \phi_B e^{\alpha t + i k x})^2 (A_e + \phi_A e^{\alpha t + i k x}) + 1 \\ &\quad - (A_e + \phi_A e^{\alpha t + i k x}) - k^2 \phi_A e^{\alpha t + i k x} \\ &= - (B_e^2 A_e + B_e^2 \phi_A e^{\alpha t + i k x} + 2 A_e B_e \phi_B e^{\alpha t + i k x} + o(2)) + 1 \\ &\quad - (A_e + \phi_A e^{\alpha t + i k x}) - k^2 \phi_A e^{\alpha t + i k x} \\ &\implies \boxed{\alpha \phi_A = - (B_e^2 + 1 + k^2) \phi_A - 2 A_e B_e \phi_B} \end{aligned} \tag{34}$$

Similarly, From the second equation, Equation (10) \implies :

$$\begin{aligned} \alpha \phi_B e^{\alpha t + i k x} &= \tau \eta (B_e + \phi_B e^{\alpha t + i k x})^2 (A_e + \phi_A e^{\alpha t + i k x}) \\ &\quad - \tau (B_e + \phi_B e^{\alpha t + i k x}) - \frac{\tau k^2}{\epsilon^2} \phi_B e^{\alpha t + i k x} \\ &= \tau \eta (B_e^2 A_e + B_e^2 \phi_A e^{\alpha t + i k x} + 2 A_e B_e \phi_B e^{\alpha t + i k x} + o(2)) \\ &\quad - \tau (B_e + \phi_B e^{\alpha t + i k x}) - \frac{\tau k^2}{\epsilon^2} \phi_B e^{\alpha t + i k x} \\ &\implies \boxed{\alpha \phi_B = \tau \eta B_e^2 \phi_A + \tau \left(2 \eta A_e B_e - 1 - \frac{k^2}{\epsilon^2} \right) \phi_B} \end{aligned} \tag{35}$$

Canceling $e^{\alpha t + i k x}$, we get the linear system:

$$\alpha \begin{pmatrix} \phi_B \\ \phi_A \end{pmatrix} = \underbrace{\begin{pmatrix} \tau(2\eta A_e B_e - 1 - \frac{k^2}{\epsilon^2}) & \tau\eta B_e^2 \\ -2A_e B_e & -(B_e^2 + 1 + k^2) \end{pmatrix}}_M \begin{pmatrix} \phi_B \\ \phi_A \end{pmatrix}$$

References

- Ayodele, S. G., Varnik, F., & Raabe, D. (2011). Lattice Boltzmann study of pattern formation in reaction-diffusion systems. *Physical Review E*, 83(1), 016702.
- Gray, P., & Scott, S. K. (1984). Autocatalytic reactions in the isothermal, continuous stirred tank reactor: Oscillations and instabilities in the system $A + 2B \rightarrow 3B$, $B \rightarrow C$. *Chemical Engineering Science*, 39(6), 1087–1097.
- Pearson, J. E. (1993). Complex patterns in a simple system. *Science*, 261(5118), 189–192.
- Strogatz, S. H. (2015). *Nonlinear dynamics and chaos: With applications to physics, biology, chemistry, and engineering* (2nd). Westview Press.
- Turing, A. M. (1952). The chemical basis of morphogenesis. *Philosophical Transactions of the Royal Society of London. Series B, Biological Sciences*, 237(641), 37–72.

Lattice Boltzmann study of pattern formation in reaction-diffusion systems

S. G. Ayodele,¹ F. Varnik,^{1,2} and D. Raabe¹¹Max-Planck Institut für Eisenforschung, Max-Planck Straße 1, D-40237 Düsseldorf, Germany²Interdisciplinary Center for Advanced Materials Simulation, Ruhr University Bochum, Stiepelstraße 129, D-44780 Bochum, Germany

(Received 19 July 2010; revised manuscript received 24 October 2010; published 26 January 2011)

Pattern formation in reaction-diffusion systems is of great importance in surface micropatterning [Grzybowski *et al.*, *Soft Matter* **1**, 114 (2005)], self-organization of cellular micro-organisms [Schulz *et al.*, *Annu. Rev. Microbiol.* **55**, 105 (2001)], and in developmental biology [Barkai *et al.*, *FEBS Journal* **276**, 1196 (2009)]. In this work, we apply the lattice Boltzmann method to study pattern formation in reaction-diffusion systems. As a first methodological step, we consider the case of a single species undergoing transformation reaction and diffusion. In this case, we perform a third-order Chapman-Enskog multiscale expansion and study the dependence of the lattice Boltzmann truncation error on the diffusion coefficient and the reaction rate. These findings are in good agreement with numerical simulations. Furthermore, taking the Gray-Scott model as a prominent example, we provide evidence for the maturity of the lattice Boltzmann method in studying pattern formation in nonlinear reaction-diffusion systems. For this purpose, we perform linear stability analysis of the Gray-Scott model and determine the relevant parameter range for pattern formation. Lattice Boltzmann simulations allow us not only to test the validity of the linear stability phase diagram including Turing and Hopf instabilities, but also permit going beyond the linear stability regime, where large perturbations give rise to interesting dynamical behavior such as the so-called self-replicating spots. We also show that the length scale of the patterns may be tuned by rescaling all relevant diffusion coefficients in the system with the same factor while leaving all the reaction constants unchanged.

DOI: 10.1103/PhysRevE.83.016702

PACS number(s): 47.11.-j, 05.10.-a, 82.40.Ck, 82.20.-w

I. INTRODUCTION

Spatially and/or temporally varying patterns have been observed in a variety of physical [1,2], chemical [3–5], and biological [6–11] systems operating far from equilibrium. The interest in understanding the physics of pattern formation in these systems has been increasing steadily over the last few years, especially after the experimental verification of Turing's idea [12]. In chemical and biological systems, for instance, macroscopic reaction-diffusion equations have been proposed as models for morphogenesis [13], pattern formation [6,7], and self-organization [14,15]. This class of equations usually includes the following two features: (i) a nonlinear reaction between chemical species describing local production or consumption of the species, and (ii) the diffusive transport of these species due to density gradients. The simple form of the reaction-diffusion equation for a system of N species is described by the following set of equations:

$$\frac{\partial \rho_s(\mathbf{x}, t)}{\partial t} = D_s \Delta \rho_s(\mathbf{x}, t) + R_s, \quad 1 \leq s \leq N, \quad (1)$$

where $\rho_s(\mathbf{x}, t)$ is the mass density or concentration of species s at time t and location \mathbf{x} , Δ is the Laplacian operator with respect to spatial coordinate \mathbf{x} , and D_s is the diffusion coefficient of individual species s . In this work, we assume that D_s is isotropic and independent of \mathbf{x} . The last term on the right hand side, R_s , is the reaction term. This term depends on the local density or concentration of the individual reacting species and the reaction mechanism governing the system. In most pattern forming systems, R_s usually contains nonlinear or autocatalytic reaction terms with the product of the densities of the reacting species.

Due to their great importance both in biology, environmental science, and industry, there has been growing interest in a

study of these systems both experimentally, by numerical integration of the governing equations, and via well-tuned analytic theories (see, e.g., [16–22] and references therein). However, solving problems with complex geometry (as is sometimes the case in biological systems) often requires a more efficient and robust method. The lattice Boltzmann method has met significant success in simulating a wide range of phenomena in complex geometries over the last decades [23–27]. In contrast with other traditional numerical techniques which only focus on the solution of the governing macroscopic equation, the lattice Boltzmann (LB) method is based on kinetic theory. In cell-scale modeling of micro-organisms [28–30], for instance, the kinetic nature of the lattice Boltzmann method makes the approach computationally less demanding and allows for a relatively simple implementation of microbial interactions between cells. Furthermore, for problems involving large domain sizes, the local nature of LB operations allows easier implementation on parallel computational platforms thus enabling fast and large scale computations. In addition to the above features, the inherent capability of the LB approach in dealing with irregular boundaries makes it suitable for studying reaction-diffusion phenomena in porous media [31] at the pore scale. However, the accuracy and efficiency of a numerical method are often evaluated in terms of the smallest truncation error within the method. In previous lattice Boltzmann studies of reaction-diffusion equation [32,33], it is rather unclear as to how the truncation error varies with the system parameters such as reaction rate and diffusion constant. These parameters become important in pattern forming systems where nonlinear reaction terms are present and reaction rate as well as diffusion constant may vary over a wide range. Thus for a better performance and accuracy, it is important to find out whether there is a range of optimal parameters that leads to the smallest truncation error and a better convergence of the method. Such

a study is performed in this work for the case of a single species reaction-diffusion systems. Performing a third-order Chapman-Enskog multiscale expansion, we investigate the dependence of the truncation error on the system parameters. Indeed, for this simple case, while the truncation error linearly varies with the reaction rate, it exhibits a pronounced minimum as a function of the diffusion coefficient.

In order to extend the investigation to a pattern-forming multispecies reaction-diffusion model, we have selected the Gray-Scott model [34], which serves as a standard paradigm for studying reaction-diffusion systems. The Gray-Scott model, though simple, exhibits a wide range of interesting dynamical features including spots [35], spiral waves [36], stationary waves [37], and spatiotemporal chaos [38]. A particular feature of this model which makes it different from the other models is the existence of the so-called self-replicating spots [39]. Spatially localized cell-like structures grow, deform, and make replicas of themselves. This act of “cell division” resembling DNA and RNA replication in cells or the replication growth of biological cells as seen in developmental biology makes it an ideal model for studying these biological systems with regard to pattern formation. In this reaction-diffusion system, generation of patterns comes usually from the instability of an initially uniform state to spatially inhomogeneous perturbations over a certain range of wavelengths. The possible range of wavelengths, as determined by a fixed set of system parameters, is usually invariant against a change of the system size. A change in system size often leads to a corresponding change in the number of spots, stripes, or segments observed in the system. Hence the number of segments or stripes is not invariant, but proportional to the system size. In contrast, for some biological systems, the pattern-forming wavelength is often proportional to the system size, while the number of stripes or segments is invariant against the change of system size. For instance, some mammalian coat markings have been shown to enlarge in proportion to system size [40], patterns in some micro-organisms like *Hydra* and *Dictyostelium discoideum* have also been observed to show proportionality with size [41]. Modeling this type of biological systems with Turing-type reaction-diffusion therefore requires rendering the governing equations dimensionless and adjusting the system parameters in a proper way [42,43]. One such approach involves using diffusion constants which depend on the concentration of a system-size-dependent auxiliary chemical factor [44–47] or using the possibility that the concentration of some chemical species changes with some power of the system size [48]. Interestingly, it is possible to change the length scale of the patterns in the Gray-Scott model via a simple rescaling of all the involved diffusion coefficients by the same factor, while keeping all the reaction constants unchanged. We provide a test of the validity of this simple approach with lattice Boltzmann simulations.

The paper is organized as follows. In the following section, we briefly introduce the lattice Boltzmann simulation scheme for the reaction-diffusion equation. We then provide some benchmark tests for our LB simulation by comparing our results with analytical solutions for the transformation reaction and diffusion of a point source in a domain with periodic boundary conditions. Excellent agreement with the analytical

solutions is found. We also carry out a truncation error analysis of the model via a third-order multiscale expansion. Results obtained from this analysis are in agreement with our numerical simulations. In Sec. III, we present the Gray-Scott model and, using linear stability analysis, determine the parameter range for the existence of unstable solutions which we identify as a necessary condition for pattern formation. Our numerical simulations show good agreement with the predictions obtained from linear stability analysis. In Sec. IV we present a detailed study of the patterns which may be obtained via large amplitude perturbations of a linearly stable state. This case comprises the self-replicating spots.

II. NUMERICAL MODEL AND ITS VALIDATION

A. Lattice Boltzmann method

The lattice Boltzmann method [49–52] can be regarded as a mesoscopic particle based numerical approach allowing us to solve fluid-dynamical equations in a certain approximation, which (within, e.g., the so-called diffusive scaling, i.e., by choosing $\Delta t = \Delta x^2$) becomes exact as the grid resolution is progressively increased. The density of the fluid at each lattice site is accounted for by a one particle probability distribution $f_i(\mathbf{x}, t)$, where \mathbf{x} is the lattice site, t is the time, and the subscript i represents one of the finite velocity vectors \mathbf{e}_i at each lattice node. The number and direction of the velocities are chosen such that the resulting lattice is symmetric so as to easily reproduce the isotropy of the fluid [53]. During each time step, particles stream along velocity vectors \mathbf{e}_i to the corresponding neighboring lattice site and collide locally, conserving mass and momentum in the process. The LB equation describing propagation and collision of the particles is given by

$$f_i(\mathbf{x} + \mathbf{e}_i, t + 1) - f_i(\mathbf{x}, t) = \Omega_i f_i(\mathbf{x}, t), \quad (2)$$

where Ω_i is the collision operator.

The most widely used variant of LB is the lattice Bhatnagar-Gross-Krook (BGK) model [51], which approximates the collision step by a single time relaxation toward a local equilibrium distribution f_i^{eq} . The lattice BGK model is written as

$$f_i(\mathbf{x} + \mathbf{e}_i, t + 1) - f_i(\mathbf{x}, t) = \frac{f_i^{\text{eq}}(\mathbf{x}, t) - f_i(\mathbf{x}, t)}{\tau}, \quad (3)$$

where τ is the relaxation time and the equilibrium distribution f_i^{eq} is closely related to the low Mach number expansion of the Maxwell velocity distribution given as [54]

$$f_i^{\text{eq}}(\mathbf{x}, t) = w_i \rho \left[1 + \frac{1}{c_s^2} (\mathbf{e}_i \cdot \mathbf{u}) + \frac{1}{2c_s^4} (\mathbf{e}_i \cdot \mathbf{u})^2 - \frac{1}{2c_s^2} u^2 \right]. \quad (4)$$

In Eq. (4), c_s is the sound speed on the lattice and w_i is a set of weights normalized to unity. The weights w_i and speed c_s depend in general on the dimension and the type of the lattice used. In this work, we use the two dimensional nine velocity (D2Q9) model with the sound speed c_s given as $c_s^2 = c^2/3$, where $c = \Delta x/\Delta t$ is the lattice speed. The lattice weights w_i for the D2Q9 model are given as

$$w_i = \begin{cases} 4/9 & \mathbf{e}_i = (0,0), \quad i = 0; \\ 1/9 & \mathbf{e}_i = (\pm 1,0), (0, \pm 1), \quad i = 1 \dots 4; \\ 1/36 & \mathbf{e}_i = (\pm 1, \pm 1), \quad i = 5 \dots 8. \end{cases} \quad (5)$$

In order to model the reaction-diffusion equations in the framework of a lattice Boltzmann BGK model, we introduce a multispecies distribution function $f_{i,s}$ where the subscript s runs over the number of species $s = 1 \dots N$. Here we assume that the diffusion of a given species does not depend on the concentration of other species. In other words, the species in our model do not interact among each other, except through the chemical reaction term. This assumption is physically justified since many pattern-forming systems are studied in the form of dilute solutions. At higher concentrations, however, the mutual interactions of different species shall be taken into account [55,56]. In addition, we focus on chemical reactions with diffusion as the only transport mechanism, i.e., with no effect of the solvent velocity field. Experimentally, this is a good approximation to pattern formation in a gel [57,58], where the effect of advection is largely suppressed. Thus the flow velocity \mathbf{u} in Eq. (4) can be set to zero. This leads to

$$f_{i,s}^{\text{eq}}(\mathbf{x}, t) = w_i \rho_s. \quad (6)$$

Equation (6) satisfies the requirement $\sum_{i=0}^N f_{i,s}^{\text{eq}} = \rho_s$. The chemical reaction is modeled by including a source term, R_s , in the collision step. This leads to

$$f_{i,s}(\mathbf{x} + \mathbf{e}_i, t+1) - f_{i,s}(\mathbf{x}, t) = \frac{f_{i,s}^{\text{eq}}(\mathbf{x}, t) - f_{i,s}(\mathbf{x}, t)}{\tau_s} + w_i R_s, \quad (7)$$

where τ_s is the relaxation time for species s . The source term R_s represents the rate of change of density of the species s with regard to reaction kinetics. The exact form of the relation between the reaction rate R_s and the density (concentration) of each species depends on the type of reaction being modeled. The density of the species s , ρ_s is then computed from the distribution function using $\rho_s = \sum_{i=0}^N f_{i,s}$.

Near equilibrium and in the limit of small Knudsen number (=mean free path/characteristic length of problem) the macroscopic reaction-diffusion equation can be recovered using Chapman-Enskog multiscale analysis. The detailed analysis leading to the macroscopic equation is outlined in the Appendix. The relaxation time τ_s is then found to be related to the diffusion coefficient as $D_s = c_s^2 \Delta t (\tau_s - 0.5)$.

B. A transformation reaction

We provide here a simple test of our lattice Boltzmann approach for reaction-diffusion systems and characterize the truncation error obtained with regard to system parameters. We compute the problem of diffusion of a species A undergoing an irreversible transformation or decay reaction to a species B ,



The reaction-diffusion equation describing the dynamics of species A can be written as

$$\frac{\partial \rho_A(x, y, t)}{\partial t} = D_A \Delta \rho_A(x, y, t) - \kappa_B \rho_A(x, y, t), \quad (9)$$

where $\rho_A(x, y, t)$ is the density of species A at point (x, y) and time t , D_A is the diffusion coefficient of A , κ_B is the rate of the transformation reaction, and Δ is the Laplacian operator with respect to spatial coordinates x, y . Taking ρ_{A0} as a reference

concentration, Eq. (9) can be made dimensionless by introducing the characteristic time $t_d = L^2/D_A$, which is the time for the diffusion over the dimension of the simulation box L . This choice is reasonable since L is the only characteristic length in this problem ($L_x = L_y = L$). This yields

$$\frac{\partial \tilde{\rho}_A(\tilde{x}, \tilde{y}, \tilde{t})}{\partial \tilde{t}} = \Delta \tilde{\rho}_A(\tilde{x}, \tilde{y}, \tilde{t}) - \phi^2 \tilde{\rho}_A(\tilde{x}, \tilde{y}, \tilde{t}), \quad (10)$$

where $\tilde{\rho}_A = \rho_A/\rho_{A0}$, $(\tilde{x}, \tilde{y}) = (x, y)/L$, $\tilde{t} = t/t_d$, and $\phi^2 = t_d \kappa_B = L^2 \kappa_B / D_A$. The Thiele modulus ϕ^2 compares the rate of reaction to the rate of diffusion. Transport by diffusion dominates the reaction kinetics when $\phi^2 \ll 1$, while reaction dominates when $\phi^2 \gg 1$. We proceed now to solve Eq. (10) by Fourier transformation. Using the initial condition $\tilde{\rho}_A(\tilde{x}, \tilde{y}, \tilde{t} = 0) = \delta(\tilde{x} - \tilde{x}_0) \delta(\tilde{y} - \tilde{y}_0)$, the Fourier transformation of Eq. (10) yields

$$\frac{d \hat{\rho}_A(\tilde{q}, \tilde{t})}{d \tilde{t}} = \tilde{q}^2 \hat{\rho}_A(\tilde{q}, \tilde{t}) - \phi^2 \hat{\rho}_A(\tilde{q}, \tilde{t}), \quad \hat{\rho}_A(\tilde{q}, 0) = 1, \quad (11)$$

where $\hat{\rho}_A(\tilde{q}, \tilde{t})$ is the Fourier transform of $\tilde{\rho}_A(\tilde{x}, \tilde{y}, \tilde{t})$. Integrating Eq. (11), taking the inverse Fourier transform, and slightly re-arranging the terms, one obtains

$$\tilde{\rho}_A(\tilde{x}, \tilde{y}, \tilde{t}) = \frac{1}{(4\pi\tilde{t})} \exp\left(\frac{-(\tilde{x} - \tilde{x}_0)^2 - (\tilde{y} - \tilde{y}_0)^2}{4\tilde{t}}\right) \exp(-\phi^2 \tilde{t}). \quad (12)$$

Equation (12) is the analytical solution of the problem posed by Eq. (10) on a region infinitely extended in space. In particular, it does not contain effects of periodic images of the simulation box [59]. It thus provides a satisfactory approximation to the simulated problem as long as the width of the Gaussian is small compared to the linear dimension of the simulation box, i.e., $D_A t \ll L^2$ or, equivalently, $\tilde{t} \ll 1$. Using Eq. (12), we perform a test of the present lattice Boltzmann (LB) model. For this purpose, we set up a two dimensional domain with $L = 200$ lattice units and $\rho_A(t = 0) = 1$ at the center of the simulation box ($x = x_0 = L/2, y = y_0 = L/2$), while $\rho_A(t = 0) = 0$ on all other points in the system. For the whole region of the domain, we initialize the density of the species B to zero. Periodic boundary condition is imposed along both the x and y directions. The lattice Boltzmann relaxation parameter of the species A and B is set to $\tau_A = \tau_B = 0.56$, corresponding to $D_A = D_B = 0.02$ (in LB units). The reaction rate, on the other hand, is $\kappa_B = 0.01$. These values correspond to a Thiele modulus of $\phi^2 = 2 \times 10^4$.

Results thus obtained are collected in Fig. 1(a). The plot compares, for two different times, the density profiles of species A along the x direction ($y = y_0 = L/2$) obtained from simulations to the analytical solution, Eq. (12).

In order to quantify the numerical error, we introduce the relative error E_ρ via the definition

$$E_\rho = \sqrt{\frac{\sum_{x,y} |\rho_{A,\text{an}}(x, y) - \rho_{s,\text{sim}}(x, y)|^2}{\sum_{x,y} |\rho_{A,\text{an}}(x, y)|^2}}. \quad (13)$$

Here, $\rho_{A,\text{an}}(x, y)$ is the density field obtained from the analytical solution in Eq. (12) and $\rho_{s,\text{sim}}(x, y)$ is the density field obtained from the simulation. The summation is taken over all lattice points in the domain.

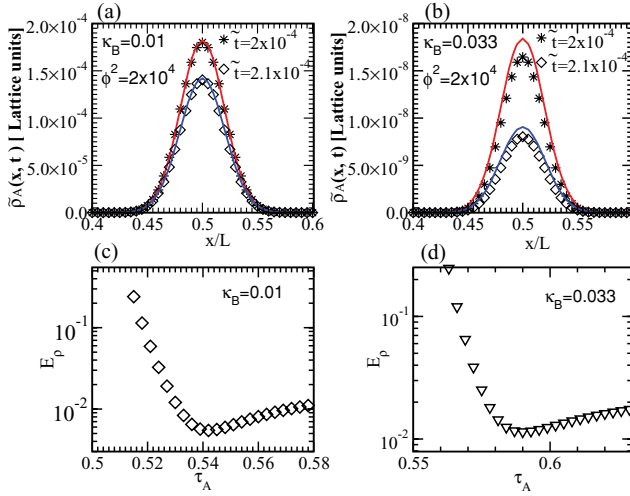


FIG. 1. (Color online) Comparison of the lattice Boltzmann simulations (symbols) with the analytical solution (solid lines) given in Eq. (12). (a) Density profiles of species A along the x direction at two different dimensionless times as indicated for $\kappa_B = 0.01$ and $\tau_A = \tau_B = 0.56$ (corresponding to $D_A = D_B = 0.02$) along the line $y = y_0$. (b) The same data as in (a) but for $\kappa_B = 0.033$. (c) Behavior of the relative error in the density of A , E_ρ [see Eq. (13)], with the relaxation parameter τ_A at $\kappa_B = 0.01$. (d) The same data as in (c) but for $\kappa_B = 0.033$. The Thiele modulus is kept constant for all the data shown here, $\phi^2 = 2 \times 10^4$. Note that a larger τ_A corresponds to a higher grid resolution, via Eq. (14).

As seen from Fig. 1(a), we obtain a good agreement between the LB simulation data and the analytical solution in Eq. (12). Using Eq. (13), this corresponds to a relative error of less than 1%. We note, however, that increasing the value of the reaction rate κ_B leads to an increase in the relative error as evident by comparing Figs. 1(a) and 1(b). We will return to this point further below.

To proceed further, we express the Thiele modulus in terms of dimensionless lattice Boltzmann parameters. For this purpose, we recall the relation between relevant physical and LB quantities, $D_A^{\text{phys}} = c_s^2 \Delta t (\tau_A - 0.5) = (\tau_A - 0.5) \Delta x^2 / (3 \Delta t)$, $\kappa_B^{\text{phys}} = \kappa_B / \Delta t$, and $L^{\text{phys}} = L \Delta x$. Note that, since all our simulation results are expressed in LB units, we have dropped—for the sake of the simplicity of notation—the superscript “LB” in all the lattice Boltzmann variables. Inserting these relations into the definition of the Thiele number, it is easy to see that

$$\phi^2 = \frac{L^{\text{phys}2} \kappa_B^{\text{phys}}}{D_A^{\text{phys}}} = \frac{3L^2 \kappa_B}{(\tau_A - 0.5)}. \quad (14)$$

A nice property of Eq. (14) is that it provides a prescription for how to change the grid resolution without changing the physical problem under investigation ($\phi = \text{const}$). In particular, in the case of the present transformation reaction and for a fixed lattice reaction rate κ_B , an increase of the grid resolution (i.e., an increase of L) must be accompanied by a corresponding increase of the LB relaxation parameter τ_A .

The reader may have noticed that the sound speed enters the Thiele modulus via a factor of 3 only. This is related to the fact that the scale of the sound speed, $\Delta x / \Delta t$, drops out

when constructing this dimensionless quantity. Indeed, effects of the sound speed on numerical accuracy are not expected to show up at this level of description, where the flow velocity is assumed to be identically zero. In the presence of flow (generated, e.g., via buoyancy forces), on the other hand, this issue may become important. A more detailed discussion of the effects of sound speed on the LB truncation error can be found in [60].

Next we systematically investigate how the relative error in the density, E_ρ , varies with the relaxation time τ_A and the reaction rate κ_B for a given physical situation. For this purpose, we first fix the Thiele modulus to $\phi^2 = 2 \times 10^4$ as in the case of Figs. 1(a) and 1(b). We then vary, for each value of the reaction rate κ_B , the relaxation parameter τ_A and determine the corresponding relative error. Note that, by doing so, the lattice resolution is automatically adapted according to Eq. (14). Results of these studies are shown in Figs. 1(c) and 1(d) for $\kappa_B = 0.01$ and $\kappa_B = 0.033$, respectively. The first observation from both curves in Figs. 1(c) and 1(d) is the existence of a minimum in the magnitude of the relative error. It is interesting that a similar minimum in the LB truncation error is also observed in the computation of shear stress [61]. Another observation is the shift in the position of the minimum of these curves with increasing reaction rate. Figure 1(c) shows that the minimum occurs at $\tau_{A,\text{min}} \approx 0.536$, for $\kappa_B = 0.01$, while increasing κ_B to 0.033 leads to $\tau_{A,\text{min}} \approx 0.59$ [Fig. 1(d)].

In order to better understand this minimum in this model and characterize the shift observed for an increasing reaction rate, we perform a third-order Chapman-Enskog expansion of the lattice Boltzmann BGK model for the reaction-diffusion equation (see the Appendix) and obtain an expression for the truncation error up to the third order in the expansion parameter ϵ . Using $R_A = -\kappa_B \rho_A$ in Eq. (A23) and rearranging the terms in powers of τ_A leads to

$$E = 3 \Delta x^2 \partial_t \partial_{x_\alpha}^2 \rho_A \left[\tau_A^2 - \left(\frac{\kappa_B \partial_t \rho_A}{3 c_s^2 \partial_t \partial_{x_\alpha}^2 \rho_A} + 1 \right) \tau_A + \frac{1}{6} \right]. \quad (15)$$

The third-order LB truncation error E is thus the product of time and spatial derivative of density with a quadratic polynomial in τ_A . This polynomial has a minimum at

$$\tau_{A,\text{min}} = \left(\frac{\kappa_B \partial_t \rho_A}{6 c_s^2 \partial_t \partial_{x_\alpha}^2 \rho_A} + 0.5 \right). \quad (16)$$

Strictly speaking, the value of $\tau_{A,\text{min}}$ not only depends on the reaction rate κ_B but also on space and time variables (through ρ_A). The fact that a minimum does indeed occur in E_ρ as a function of τ_A is therefore not at all a trivial consequence of Eq. (15). Indeed, the shape of $E_\rho(\tau_A)$ significantly deviates from a parabola suggesting that the nontrivial effects related to time and spatial derivatives of ρ_A are present.

Nevertheless, it is worth testing to which extent useful information on the behavior of LB truncation error can be gained via the above analysis. For this purpose, we note two important features, which can be extracted from Eqs. (15) and (16). The first one is that E_ρ could be a linear function of the reaction rate κ_B [see Eq. (15)]. The second observation is that also the position of the minimum in $E_\rho(\tau_A)$, i.e. the value of $\tau_{A,\text{min}}$ could be a linearly increasing function of κ_B .

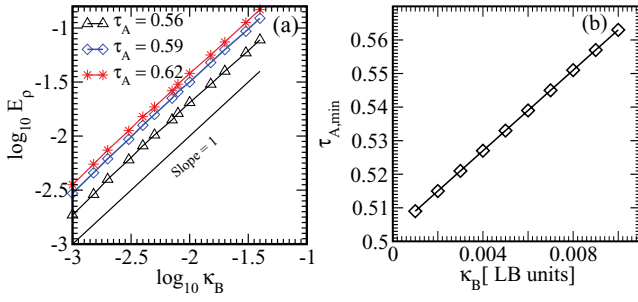


FIG. 2. (Color online) (a) Log-log plot of E_ρ vs κ_B for different values of τ_A . The curves are parallel to the solid black line with a slope of 1. (b) Plot of $\tau_{A,\min}$ vs κ_B . The curve is in line with Eq. (16).

As illustrated in Fig. 2, both these predictions are confirmed by our lattice Boltzmann simulations. Moreover—even though not exactly—the position of the minimum error tends toward the predicted limit of $\tau_{A,\min} = 0.5$ as $\kappa_B \rightarrow 0$ [Fig. 2(b)]. In summary, given a physical system (i.e., for constant physical parameters such as reaction rate and diffusion coefficient) the above discussion may provide guidance in choosing an optimum grid resolution, when seeking a compromise between computational cost and numerical accuracy.

III. GRAY-SCOTT MODEL

We consider next the Gray-Scott model as a typical example of a two species reaction-diffusion system where the nonlinear reaction terms between the species coupled with the transport by diffusion give rise to spatiotemporal patterns. The Gray-Scott model describes the kinetics of a simple autocatalytic reaction in an unstirred homogeneous flow reactor [34]. The reactor is confined in a narrow space between two porous walls in contact with a reservoir. Substance A whose density is kept fixed at A_0 in the reservoir outside of the reactor is supplied through the walls into the reactor with the volumetric flow rate per unit volume k_f . Inside the reactor, A undergoes an autocatalytic reaction with an intermediate species B at a rate k_1 . The species B then undergoes a decay reaction to an inert product C at a rate k_2 . The product C and excess reactants A and B are then removed from the reactor at the same flow rate per unit volume k_f . The basic reaction steps are summarized as follows:



The reaction in Eq. (17) is the cubic autocatalytic reaction in which two molecules of species B produce three molecules of B through interaction with the species A . The presence of B stimulates further production of itself, while the presence of A controls the production of B . Substance A is sometimes called the inhibitor and B the activator. By constantly feeding the reactor with a uniform flow of species A while at the same time removing the product and excess reactants, far from equilibrium conditions can be maintained. Note that inside the reactor the two species A and B are assumed to interact only through the nonlinear autocatalytic reaction in Eq. (17). In

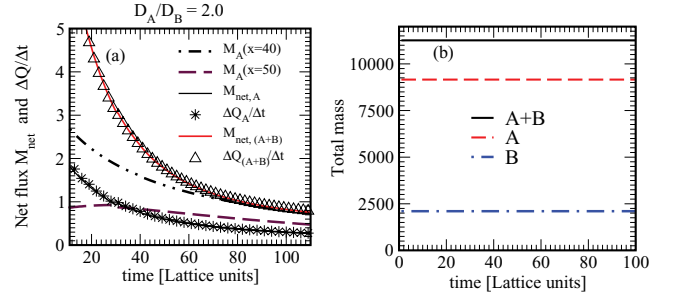


FIG. 3. (Color online) Test of the continuity equation within a stripe defined by two vertical lines at $x_1 = 40$ and $x_2 = 50$. (a) The mass fluxes across x_1 and x_2 are not identical: $M_A(x = 40) \neq M_A(x = 50)$, where $M_A(x) = \sum_{y=0}^{L_y} J_A(x, y)$ and $J_A = \sum_i f_{i,A} c_{i,x}$. This implies that the mass within the domain must change with time ($\Delta Q_A/\Delta t \neq 0$). However, as expected from the continuity equation, this rate of change is identical to the net mass flux across the boundaries of the domain, $M_{\text{net},A}(t) = M_A(x_1) - M_A(x_2)$. Note that, here, we define $M_{\text{net},A}$ as “inflow (at x_1) minus outflow (at x_2).” Similarly, the sum of the masses of the species A and B within the stripe also changes with time without violating the continuity equation. (b) The total mass within the entire simulation box vs time for the species A and B . The initial configuration is identical to that of Figs. 10 (a square box of high concentration of B within an A -rich domain). All the reaction rates are set to zero.

particular, interaction terms due to cross diffusion between the species are neglected. As stated before, this assumption is physically justified as pattern-forming systems often occur in the form of dilute solutions. Following this assumption, the equations of chemical kinetics which describe the above situations and include the spatiotemporal variations of the concentrations of A and B in the reactor take the following form:

$$\frac{\partial A}{\partial t} = k_f(A_0 - A) - k_1 B^2 A + D_A \nabla^2 A, \quad (19)$$

$$\frac{\partial B}{\partial t} = -(k_f + k_2)B + k_1 B^2 A + D_B \nabla^2 B, \quad (20)$$

where A and B are the density of species A and B , respectively, A_0 is the density of A in the reservoir, while D_A and D_B are the diffusion coefficients of species A and B , respectively. Note that the full Gray-Scott model in Eqs. (19) and (20) describe chemical reaction and mass transfer in an open system and therefore it is generally not a mass-conserving system. However, by setting all the reaction terms in Eqs. (19) and (20) to zero, one recovers a purely diffusive system. In this case, it is easy to see that the system is mass conserving. This, however, does not imply that the sum of the densities of all the species at a given point in space is constant. Rather, the rate of mass change in a given area in space is identical to the net flux across the boundary of that domain. Our numerical simulations do indeed confirm this fact (Fig. 3).

In order to understand and control the relevant time scale and length scale of patterns observed in these systems, we introduce variables in the form of time and length scales that represent the physical processes acting in the system. For A , the characteristic time scale is the time for the removal of A given

as $1/k_f$ whereas for B it is $1/(k_f + k_2)$. The characteristic time and length scales for these quantities are then

$$\tau_A = 1/k_f, \quad \tau_B = 1/(k_f + k_2), \quad l_A = (D_A \tau_A)^{1/2}, \quad (21)$$

$$l_B = (D_B \tau_B)^{1/2}.$$

Please note that in contrast to Sec. II B where τ_A and τ_B are used to denote the LB relaxation parameters for the species A and B , here they denote the times associated with the reaction rates k_f and $k_f + k_2$. Furthermore, note also that the diffusion coefficients D_A and D_B in Eqs. (19) and (20) are independent of τ_A and τ_B . Rather, in an implementation within the present D2Q9-LB model, these quantities are related to the LB relaxation parameters via $D_A = (\tau_A^{\text{LB}} - 0.5)/3$ and $D_B = (\tau_B^{\text{LB}} - 0.5)/3$. Next we introduce the dimensionless quantities

$$\tilde{A} = A/A_0, \quad \tilde{B} = B/B_0, \quad B_0 = \left(\frac{k_f}{k_1}\right)^{1/2}. \quad (22)$$

Inserting the quantities in Eqs. (21) and (22) into Eqs. (19) and (20) leads to

$$\tau_A \frac{\partial \tilde{A}}{\partial t} = -\tilde{B}^2 \tilde{A} + 1 - \tilde{A} + l_A^2 \nabla^2 \tilde{A}, \quad (23)$$

and

$$\tau_B \frac{\partial \tilde{B}}{\partial t} = +\eta \tilde{B}^2 \tilde{A} - \tilde{B} + l_B^2 \nabla^2 \tilde{B}, \quad (24)$$

where the parameter $\eta = A_0(k_1 k_f)^{1/2}/(k_f + k_2)$ is the strength of the activation process. It adjusts the strength of the nonlinear term in Eq. (24).

The number of parameters can be further reduced by rescaling the time and length scale in units of τ_A and l_A , respectively. This yields

$$\frac{\partial \tilde{A}}{\partial \tilde{t}} = -\tilde{B}^2 \tilde{A} + 1 - \tilde{A} + \tilde{\nabla}^2 \tilde{A}, \quad (25)$$

$$\frac{1}{\tau} \frac{\partial \tilde{B}}{\partial \tilde{t}} = +\eta \tilde{B}^2 \tilde{A} - \tilde{B} + \frac{1}{\varepsilon^2} \tilde{\nabla}^2 \tilde{B}, \quad (26)$$

where $\tau = \tau_A/\tau_B$ and $\varepsilon = l_A/l_B = \sqrt{\tau_A D_A/\tau_B D_B}$. The parameter τ describes the relative strength of the reaction terms.

In general, Eqs. (25) and (26) are difficult to investigate by analytic means. However, simple cases exist for which analytical solutions can be found. We start with probably the most simple situation of a spatially homogeneous distribution of \tilde{A} and \tilde{B} ($\nabla^2 \tilde{A} = 0$, $\nabla^2 \tilde{B} = 0$). In this case, the steady state solutions of Eqs. (25) and (26), denoted as \tilde{A}_e and \tilde{B}_e , obey

$$-\tilde{B}_e^2 \tilde{A}_e + 1 - \tilde{A}_e = 0, \quad (27)$$

$$\eta \tilde{B}_e^2 \tilde{A}_e - \tilde{B}_e = 0.$$

Equation (27) has three solutions. The first solution is the trivial homogeneous solution $\tilde{B}_e = 0$, $\tilde{A}_e = 1$. This state exists for all system parameters. The other two solutions exist provided that $\eta > 2$. These are given by

$$\tilde{A}_e^\pm = \frac{\eta \pm \sqrt{\eta^2 - 4}}{2\eta} \quad \text{and} \quad \tilde{B}_e^\pm = \frac{\eta \mp \sqrt{\eta^2 - 4}}{2}. \quad (28)$$

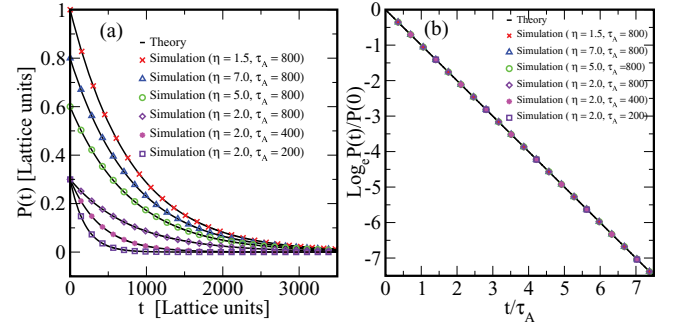


FIG. 4. (Color online) (a) A plot of $-P(t) = \eta \tilde{A}(t) + \tilde{B}(t) - \eta$ vs time for $\tau = \tau_A/\tau_B = 1$ but different values of the parameters τ_A and η as indicated. The solid black curve in each case corresponds to theoretical prediction for the parameter values used in the simulation. In all studied cases, the simulation results exponentially decay to zero and show a perfect agreement with the analytical prediction, Eq. (30). (b) Plot of $\log_e[P(t)/P(0)]$ vs t/τ_A for the same data as shown in (a).

A. Test of simulations in the case of spatially homogeneous dynamics

As a check of our simulation approach, we study the homogenized form of situations where Eqs. (25) and (26) are accessible to an analytical solution. For this purpose, we consider the case of spatially homogeneous dynamics with $\tau = 1$, implying $\tau_A = \tau_B$. In this case, multiplying Eq. (25) by η and adding the result to Eq. (26) leads to

$$\frac{d(\eta \tilde{A} + \tilde{B})}{d\tilde{t}} = \eta - (\eta \tilde{A} + \tilde{B}) \Rightarrow \frac{dP}{d\tilde{t}} = -P, \quad (29)$$

where $P = \eta \tilde{A} + \tilde{B} - \eta$ and we used the fact that $d\eta/d\tilde{t} = 0$. Equation (29) has the simple solution $P(t) = P(0) \exp(-\tilde{t}) = P(0) \exp(-t/\tau_A)$. In other words,

$$\eta \tilde{A}(t) + \tilde{B}(t) - \eta = [\eta \tilde{A}(0) + \tilde{B}(0) - \eta] \exp(-t/\tau_A). \quad (30)$$

A test of Eq. (30) is provided in Fig. 4 for $\tau = 1$ but different values of the parameters τ_A and η . In the case where $\eta < 2$, the simulation starts from a spatially homogeneous state $\tilde{A}(0) = 1$, $\tilde{B}(0) = 0$ with an additional density fluctuation $\delta A = 0.5$ and $\delta B = 0.25$ added homogeneously to A and B , respectively. This is done to break the symmetry which would keep the system at the initial state (due to the autocatalytic nature of the Gray-Scott model, without B , no reaction will take place). For all other cases where $\eta \geq 2$ we start from the nontrivial states $(\tilde{A}_e^\pm, \tilde{B}_e^\pm)$ given by Eq. (28) with an additional small fluctuation of the form $\delta A = 0.1$ and $\delta B = 0.1$. For all values of τ_A and η investigated, we found that the error between theory and simulation is well below 0.2%.

B. Stability analysis of spatially homogeneous states

We proceed in this section to determine the stability of the stationary and homogeneous solutions obtained in Eq. (28) with regard to a spatially homogeneous perturbation. Our analysis starts by looking at the growth rate α of an infinitesimal perturbation about the steady state,

$$\tilde{A} = \tilde{A}_e + \phi_A e^{\alpha t}, \quad \tilde{B} = \tilde{B}_e + \phi_B e^{\alpha t}, \quad (31)$$

where ϕ_A and ϕ_B are the amplitude of the perturbation to the species A and B , respectively. Substituting Eq. (31) into Eqs. (25) and (26), after linearizing and re-arrangement of the terms one arrives at the eigenvalue equation

$$(\mathbf{J} - \alpha \mathbf{I}) \phi = 0, \quad (32)$$

where \mathbf{I} is the identity matrix, $\phi = (\phi_A, \phi_B)^T$, and the matrix \mathbf{J} is given as

$$\mathbf{J} = \begin{bmatrix} \tau(2\eta\tilde{A}_e^\pm\tilde{B}_e^\pm - 1) & \tau\eta\tilde{B}_e^{\pm 2} \\ -2\tilde{A}_e^\pm\tilde{B}_e^\pm & -(\tilde{B}_e^{\pm 2} + 1) \end{bmatrix}. \quad (33)$$

The eigenvalue equation in Eq. (32) has the characteristic polynomial

$$\alpha^2 - \alpha \text{tr} \mathbf{J} + |\mathbf{J}| = 0, \quad (34)$$

where $\text{tr} \mathbf{J}$ and $|\mathbf{J}|$ are the trace and determinant of matrix \mathbf{J} . The pair of solutions or eigenvalues of matrix \mathbf{J} is written

$$\alpha_{1,2} = \frac{1}{2}(\text{tr} \mathbf{J} \pm \sqrt{(\text{tr} \mathbf{J})^2 - 4|\mathbf{J}|}). \quad (35)$$

The eigenvalues $\alpha_{1,2}$ in Eq. (35), can either be real or complex conjugate depending on the relative magnitude and sign of the determinant $|\mathbf{J}|$ and trace $\text{tr} \mathbf{J}$. If the real part of at least one eigenvalue is positive, the considered solution is unstable.

For the trivial state ($A_e = 1, B_e = 0$), $\text{tr} \mathbf{J} = (\tau + 1)$ and $|\mathbf{J}| = \tau$. Using Eq. (35) and the fact that $\tau > 1$ one obtains that both eigenvalues are negative. Hence this state is linearly stable with respect to spatially homogeneous perturbations. Next we consider the nontrivial stationary homogeneous solutions. In this case, inserting the solutions of A_e^\pm and B_e^\pm given in Eq. (28) in Eq. (33), one obtains that $\text{tr} \mathbf{J} = (\tau - \eta\tilde{B}_e^\pm)$ and $|\mathbf{J}| = \tau(\eta\tilde{B}_e^\pm - 2)$. Furthermore, since in this case $\eta > 2$, and using Eq. (28), one can easily verify that $|\mathbf{J}|(\tilde{B}_e^+) = (\eta\tilde{B}_e^+ - 2) < 0$ and $|\mathbf{J}|(\tilde{B}_e^-) = (\eta\tilde{B}_e^- - 2) > 0$. Now from Eq. (35) it follows that, independent of the sign of $\text{tr} \mathbf{J}$, one of the solutions $\alpha_{1,2}$ is always positive, provided that $|\mathbf{J}| < 0$. Hence the state \tilde{B}_e^+ is always unstable. For the state \tilde{B}_e^- , on the other hand, both solutions $\alpha_{1,2}$ will have the same sign as $\text{tr} \mathbf{J}$ and thus the state \tilde{B}_e^- may be stable provided $\text{tr} \mathbf{J} < 0$ (i.e., $\tau < \eta\tilde{B}_e^-$).

Figure 5 shows a typical bifurcation diagram for the system. We plot the homogeneous steady state solutions obtained in Eq. (28) as a function of the control parameter η . For $\eta < 2$ there exists only the trivial state (1,0), while when $\eta > 2$ two additional states, $(\tilde{A}_e^-, \tilde{B}_e^-)$ and $(\tilde{A}_e^+, \tilde{B}_e^+)$, emerge. The state $(\tilde{A}_e^+, \tilde{B}_e^+)$ is always unstable (indicated by a dashed line) while the state $(\tilde{A}_e^-, \tilde{B}_e^-)$ is stable if $\tau < \eta\tilde{B}_e^-$. In the same figure we have also plotted the steady state solutions obtained from the lattice Boltzmann simulation of the spatially homogeneous solutions with small homogeneous perturbations at time $t = 0$. As seen in Fig. 5, the LB simulation well reproduces the analytically predicted stability diagram.

C. Inhomogeneous state and Turing instability

The Gray-Scott model develops a Turing instability for a range of parameters. In this region of the parameter space

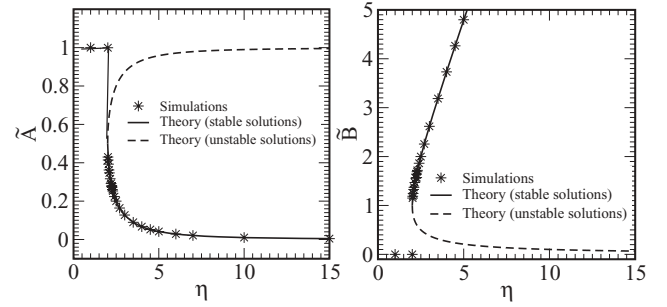


FIG. 5. Plot of the stationary homogeneous state solutions of species A and B given by Eq. (28). Above the bifurcation point ($\eta = 2.0$), two solutions exist: one is unstable to homogeneous perturbations (indicated as a dashed line) and the other may be stable (plotted as a solid line). At $\eta = 2.0$, the stable solution switches to the trivial homogeneous state (1,0) and for $\eta < 2.0$ only the trivial state exists. The lattice Boltzmann simulation (indicated by symbols) shows good agreement with the theory.

the homogeneous steady state solution becomes unstable and a new stationary but inhomogeneous state characterized by the formation of patterns becomes stable. We examine the condition for Turing instability in this system by looking at the growth rate α of an infinitesimal spatially inhomogeneous perturbation to the steady state solutions,

$$\tilde{A} = \tilde{A}_e + \phi_A e^{\alpha t} e^{i\tilde{q}x}, \quad \tilde{B} = \tilde{B}_e + \phi_B e^{\alpha t} e^{i\tilde{q}x}. \quad (36)$$

As in the case of Eq. (31), ϕ_A and ϕ_B are the amplitude of the perturbations to the species A and B respectively, and q is the wave number. Again, inserting Eq. (36) into the kinetic Eqs. (25) and (26) and after linearizing and slight re-arrangement one arrives at the eigenvalue equation

$$(\mathbf{M} - \alpha \mathbf{I}) \phi = 0, \quad (37)$$

where the matrix \mathbf{M} is written as

$$\mathbf{M} = \begin{bmatrix} \tau(2\eta\tilde{A}_e^\pm\tilde{B}_e^\pm - 1 - \frac{\tilde{q}^2}{\epsilon^2}) & \tau\eta\tilde{B}_e^{\pm 2} \\ -2\tilde{A}_e^\pm\tilde{B}_e^\pm & -(\tilde{q}^2 + \tilde{B}_e^{\pm 2} + 1) \end{bmatrix}. \quad (38)$$

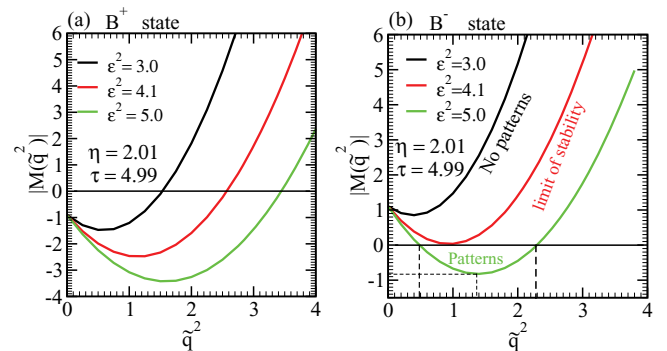


FIG. 6. (Color online) The plot of $|\mathbf{M}(\tilde{q}^2)|$ vs \tilde{q}^2 for states (a) B_e^+ (b) B_e^- . These plots show the range of growth modes q for which the determinant $|\mathbf{M}(\tilde{q}^2)|$ is negative with the possibility of pattern formation.

For the trivial solution ($A_e = 1, B_e = 0$) the matrix M reduces to

$$\mathbf{M} = \begin{bmatrix} -\tau(1 + \frac{\tilde{q}^2}{\varepsilon^2}) & 0 \\ 0 & -(\tilde{q}^2 + 1) \end{bmatrix}, \quad (39)$$

and solving the eigenvalue equation in Eq. (37), we obtain the eigenvalues of the trivial state as $\alpha_1 = -\tau(1 + \tilde{q}^2/\varepsilon^2)$ and $\alpha_2 = -(\tilde{q}^2 + 1)$. Since both eigenvalues are negative, the trivial homogeneous state ($A_e = 1, B_e = 0$) is linearly stable for all system parameters, and independent of the wavelength of the applied perturbation. However, it is important to emphasize that this stability is restricted to infinitesimal perturbations. Indeed, the trivial state is found to be unstable with respect to large amplitude spatially inhomogeneous perturbations. In fact, it is in this regime that the so-called self-replicating spots are observed. The original parametrization of the Gray-Scott model by Pearson [34] is also based on the numerical simulation of spatially inhomogeneous perturbations of the trivial state.

For the remaining nontrivial solutions, we insert the homogeneous steady state solutions $\tilde{A}_e^\pm = 1/(\eta\tilde{B}_e^\pm)$ into the matrix \mathbf{M} in Eq. (38) and solve for the eigenvalues of \mathbf{M} with the characteristic Eq. (34) by replacing \mathbf{J} with $\mathbf{M}(q)$. The corresponding eigenvalues are then obtained from Eq. (35) by replacing $\text{tr} \mathbf{J}$ and $|\mathbf{J}|$ with $\text{tr} \mathbf{M}(q^2) = \tau - \eta\tilde{B}_e^\pm - \tilde{q}^2(\tau/\varepsilon^2 + 1)$ and $|\mathbf{M}(q^2)| = \tilde{q}^4\tau/\varepsilon^2 + \tilde{q}^2(\tau\eta\tilde{B}_e^\pm/\varepsilon^2 - \tau) + \tau(\eta\tilde{B}_e^\pm - 2)$, respectively.

Turing structures or patterns emerge when the system becomes unstable with respect to inhomogeneous perturbations. Again, at least one of the eigenvalues becomes positive (unstable), when $|\mathbf{M}(q^2)| < 0$. $|\mathbf{M}(q^2)|$ is a parabola in q^2 which attains its minimum value for

$$q_{\min}^2 = \frac{(\varepsilon^2 - \eta\tilde{B}_e^\pm)}{2}. \quad (40)$$

Since $q^2 > 0$, a minimum in $|\mathbf{M}(q^2)|$ exists only if $\varepsilon^2 > \eta\tilde{B}_e^\pm$. This is one of the conditions for Turing instability in this system. The boundary of the instability band or range of wave number q for which $|\mathbf{M}(q^2)| < 0$ is given by the roots of the equation $|\mathbf{M}(q^2)| = 0$:

$$q_{1,2}^2 = \frac{-(\eta\tilde{B}_e^\pm - \varepsilon^2) \pm \sqrt{(\eta\tilde{B}_e^\pm - \varepsilon^2)^2 - 4\varepsilon^2(\eta\tilde{B}_e^\pm - 2)}}{2}. \quad (41)$$

In Eq. (41), there is an important observation concerning the state B_e^+ . Using $\eta > 2$ and Eq. (28) one can show that for the state B_e^+ , the condition $\eta\tilde{B}_e^+ < 2$ holds for all $\eta > 2$. The consequence is that Eq. (28) has always one negative root and one positive root independent of the value of ε^2 . Since $|\mathbf{M}(q^2)| < 0$ for $q = 0$ [see Fig. 6(a)], this opens already an instability band for pattern formation as regards the state B_e^+ . On the other hand, for the state B_e^- , two distinct positive real roots are necessary for an instability band of patterns. Thus the following condition has to be satisfied:

$$\eta\tilde{B}_e^- < \varepsilon^2 < -8 + 11.65\eta\tilde{B}_e^- \text{ (Turing space)}. \quad (42)$$

The first condition, $\varepsilon^2 > \eta\tilde{B}_e^-$ as discussed above, is necessary for the formation of Turing patterns while the second one reflects the requirement of a positive discriminant in

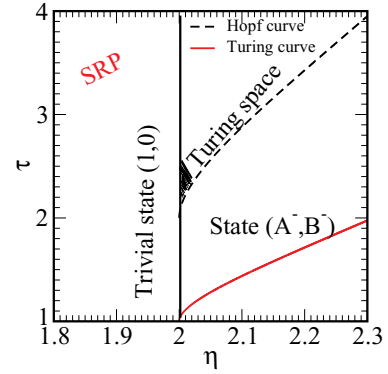


FIG. 7. (Color online) The phase diagram of the model at $D_A/D_B = 2$ showing the Turing curve and the Hopf curve for parameter space spanned by τ and η . For $\eta < 2$ only the trivial state exists and the self-replicating spots (SRP) are observed in this regime only. For $\eta > 2$ two additional states (A_e^\pm, B_e^\pm) emerge. In this figure we have only shown the states (A_e^-, B_e^-). The majority of the patterns formed from the B^- state in our lattice Boltzmann simulations are observed in the shaded region of the Turing space.

Eq. (41). Using the definition of ε^2 the first condition can be re-written as

$$\frac{l_A^2}{l_B^2} > \eta\tilde{B}_e^-. \quad (43)$$

This means that the diffusive length scale for the species A ($l_A = \sqrt{D_A\tau_A}$) must be at least $\eta\tilde{B}_e^-$ times larger than that of B ($l_B = \sqrt{D_B\tau_B}$). In other words, for a given value of parameter τ , the diffusion coefficient of species A has to be $(\eta\tilde{B}_e^-/\tau)$ times larger than that of B . In η and τ parameter space, the curves $\tau = (D_B/D_A)\eta\tilde{B}_e^-$ and $\tau = (D_B/D_A)(-8 + 11.65\eta\tilde{B}_e^-)$ define the limits of stability with respect to Turing patterns. The first curve $\tau = (D_B/D_A)\eta\tilde{B}_e^-$ is plotted as the Turing curve in Fig. 7 for $D_A/D_B = 2$. The second curve $\tau = (D_B/D_A)(-8 + 11.65\eta\tilde{B}_e^-)$ lies above the first curve and falls outside the plotted range. It is therefore not shown in the figure. At zero mode ($q = 0$), another important instability known as the Hopf instability occurs when the real part of a pair of complex eigenvalues passes through zero. In other words, a Hopf instability characterizes the transition from a decaying oscillating mode [$\text{tr} \mathbf{M}(0) < 0$] to an oscillation with growing amplitude [$\text{tr} \mathbf{M}(0) > 0$]. Thus the limit of Hopf instability is given by the condition $\text{tr} \mathbf{M}(0) = 0$. The dashed black line in Fig. 7 indicates the limit of the Hopf instability. The small dashed area in the Turing space is the region where most patterns are expected to be observed.

D. Lattice Boltzmann simulation of the spatially inhomogeneous dynamics

In this section we perform lattice Boltzmann simulations of the Gray-Scott model for different values of parameters τ and η . Here our simulation and parametrization is based on the nontrivial states (A_e^\pm, B_e^\pm). Starting from the homogeneous steady state (A_e^-, B_e^-), we apply a small amplitude density fluctuation of the form $\delta\rho = \phi \cos(q_x x) \cos(q_y y)$ where ϕ is the amplitude given and q is the wave number of the perturbations. We have chosen $\phi = 0.01$ and $q_x = q_y = 1$ in

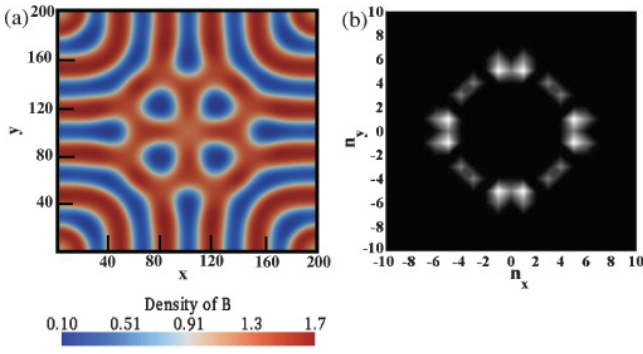


FIG. 8. (Color online) (a) Spatial distribution of the density \tilde{B} at time $t = 400\,000$, $\eta = 2.0139$, and $\tau = 2.7330$. The formation of stripes can be observed at these parameters. (b) Amplitude of the Fourier components of density fluctuation ($\tilde{B} - \tilde{B}_e$) at time $t = 400\,000$, as a function of the wave vector $q = 2\pi[(n_x/L_x)^2 + (n_y/L_y)^2]^{1/2}$. The dimensionless density \tilde{B}_e corresponds to the unstable homogeneous state for the selected set of parameters η and ϵ . The white region in the Fourier spectrum corresponds to the excited wave numbers (n_x, n_y) .

the simulations. Figure 8(a) shows a developed stable structure from the small amplitude initial perturbation to the B^- state with parameters $\eta = 2.014$ and $\tau = 2.733$. For the purpose of comparison with the prediction of linear stability analysis, we perform the Fourier transform of the pattern in Fig. 8(a) and calculate the excited wave numbers in the Fourier spectrum using the relation

$$q = 2\pi[(n_x/L_x)^2 + (n_y/L_y)^2]^{1/2}, \quad (44)$$

where n_x and n_y satisfy $-L_x/2 < n_x < L_x/2$ and $-L_y/2 < n_y < L_y/2$, respectively.

The Fourier spectrum is shown in gray scale in Fig. 8(b) and the excited wave numbers are $(n_x, n_y) \in \{(\pm 1, \pm 5); (\pm 3, \pm 4); (\pm 4, \pm 3); (\pm 5, \pm 1)\}$. Using these values of n_x and n_y in Eq. (44) to calculate q and the parameters $\eta = 2.0139$ and $\epsilon^2 = 5.466$ in Eq. (41), we found that all the excited wave numbers from the simulation fall within the instability band predicted by linear stability analysis in Eq. (41). This provides a further validation of our lattice Boltzmann simulation with regard to this model.

By performing a number of similar simulations with different values of τ and η , we have found that Turing patterns develop over some part of the region where the B^- state is Hopf or Turing unstable (indicated as the Turing space in Fig. 7). The panels in Fig. 9 show developed stationary structures for typical values of the parameters η and τ . These parameter values fall between the saddle node bifurcation curve ($\eta = 2$) and the Turing curve (see Fig. 7). One observation from Fig. 9 is that increasing the value of η within the Turing regime leads to the development of a lacelike structure in the patterns.

IV. BEYOND LINEAR STABILITY: SELF-REPLICATING SPOTS

In this section, a further example is provided for the maturity of the lattice Boltzmann method in studying pattern formation within the Gray-Scott model. The patterns discussed so far

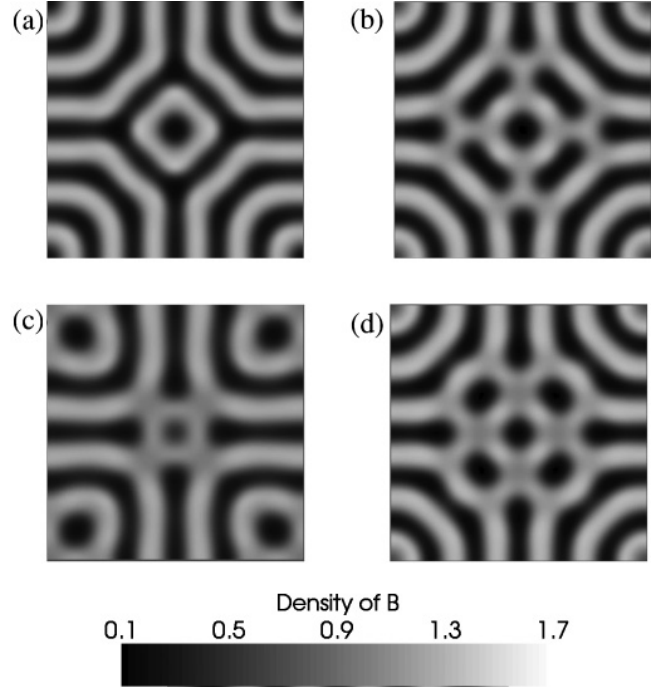


FIG. 9. Stable time independent Turing structures developed from infinitesimal perturbations to state (A_e^-, B_e^-) at parameters (a) $\eta = 2.007\,281\,9$, $\tau = 2.742\,424$, (b) $\eta = 2.013\,958$, $\tau = 2.733\,33$, (c) $\eta = 2.017\,971$, $\tau = 2.707\,462$, and (d) $\eta = 2.018\,433\,6$, $\tau = 2.7272$. The system size in all cases considered above is 200×200 lattice units.

are in the part of the phase diagram (Fig. 7), where linear stability analysis predicts that homogeneous solutions are unstable with respect to small perturbations. There are also other types of structures, which occur in a regime, where the trivial homogeneous state is linearly stable. These patterns emerge only if the homogeneous state is perturbed strongly enough. A prominent example of this type of structure are the so-called self-replicating spots.

Figure 10 illustrates the patterns emerging from a finite amplitude perturbation of the trivial state. The starting configuration corresponds to a rectangular box of species A and B with densities $\tilde{A} = 0.5$, $\tilde{B} = 0.25$ placed at the center of a domain filled with species A and B at densities $\tilde{A} = 1.0$, $\tilde{B} = 0$, respectively. Obviously, such an initial state represents a strong perturbation of the trivial state ($\tilde{A} = 1$, $\tilde{B} = 0$, i.e., $A = A_0$, $B = 0$). The sequence of images in Fig. 10 demonstrates how spots form, elongate, and then replicate as time proceeds. This self-replication process continues until the whole simulation cell is filled with the spots. Interestingly, the number of spots increases with time, while the size of an individual spot seems to remain roughly constant. We have repeated this simulation for a larger box size but otherwise exactly the same parameters. The result of this study is also shown in Fig. 10. As seen from the last image in Fig. 10, the size of a spot does not change, but only the number of spots increases to fill the entire simulation cell.

In the light of the above presented results, one may raise the question of whether it is possible to keep the number of spots constant but tune their size. An answer to this question

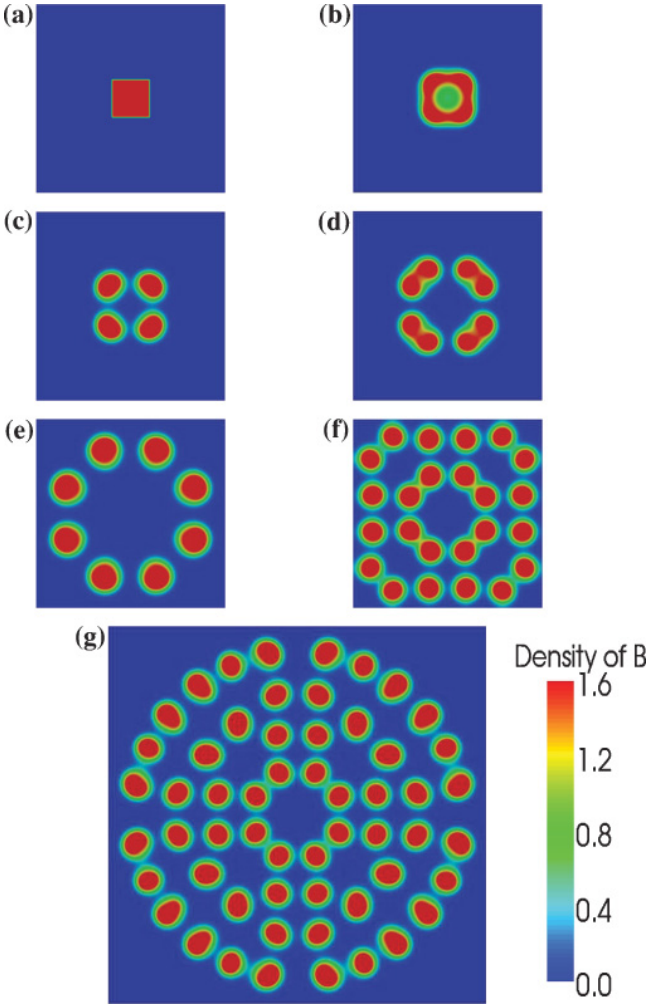


FIG. 10. (Color online) Snapshots of the density distribution of species B showing different stages in the self-replication process at times (a) $t = 0$, (b) $t = 10\,000$, (c) $t = 20\,000$, (d) $t = 50\,000$, (e) $t = 100\,000$, (f) $t = 300\,000$ with size 200×200 lattice units, and (g) $t = 300\,000$ with size 400×400 lattice units.

is obtained by noting that the dynamics of Eqs. (25) and (26) depends only on the dimensionless quantities ε , τ , and η . In other words, we must check whether it is possible to tune the length scale of the problem without altering the values of these dimensionless parameters. This would ensure that the thus-obtained new solution will have exactly the same shape (and thus the same number of spots) but a different length scale (different size spots). Indeed, a look at parameter ε reveals that it is equal to the ratio of two characteristic lengths l_A and l_B , $\varepsilon = l_A/l_B = \sqrt{\tau_A D_A / \tau_B D_B}$. Thus if we multiply both l_A and l_B by a constant factor λ , the parameter ε remains unchanged. Furthermore, in order to keep also the other two parameters τ and η constant, the simplest choice to achieve such a change of length scale is via diffusion coefficient, i.e., via $D_A \rightarrow \lambda^2 D_A$ and $D_B \rightarrow \lambda^2 D_B$.

In order to test the above idea, we design two systems such that system 1 has a linear dimension of $L_1 = 200$ lattice units with diffusion coefficients $D_{A,1} = 0.016\Delta x^2/\Delta t$ and $D_{B,1} = 0.008\Delta x^2/\Delta t$. For system 2, we choose $L_2 = 400$ lattice units, which means that $\lambda = 2$. Following the above

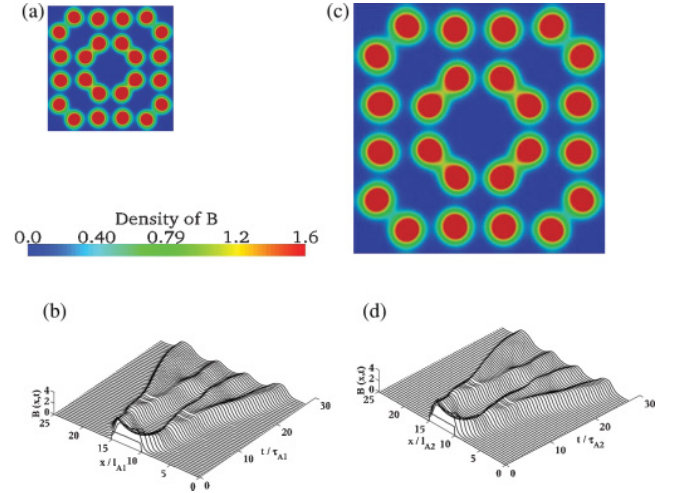


FIG. 11. (Color online) Snapshot of the spatial distribution of the density \tilde{B} showing self-replicating spots at time 300 000, $\eta = 1.86$, $\tau = 3.40$, and $\varepsilon = 2.61$ for the two systems with lattice size (a) 200×200 lattice units, (c) 400×400 lattice units. (b) and (d) show space-time plots of the density profile of the self-replicating spots along a line in the y direction for the two system sizes in (a) and (c), respectively.

arguments, we set the diffusion coefficients of species A and B in system 2 to $D_{A,2} = \lambda^2 D_{A,1} = 0.064\Delta x^2/\Delta t$, and $D_{B,2} = \lambda^2 D_{B,1} = 0.032\Delta x^2/\Delta t$, respectively. As the initial state, we perturb the trivial state exactly in the same way as described in the context of Fig. 10 and impose periodic boundary conditions in both the x and y directions. Note that the size of the square perturbation must also be multiplied by λ in conformity with the change of length scale. Results of these simulations are shown in Figs. 11(a) and 11(c). The structure of the patterns is identical for the two systems within numerical discretization errors. The inner core diameter of the spots is found to scale as the diffusion length of species A , l_A . A more quantitative comparison of the data is provided in Figs. 11(b) and 11(d), where time evolution of the density profiles is shown for both studied system sizes in a space-time plot along the x direction.

The above arguments on how to tune the length scale while keeping the shape of the patterns unchanged is quite general and applies to any other solution of the Gray-Scott model as well. Here, we provide an example from the Turing regime. This is an interesting test, as linear stability analysis predicts that when the system size is increased, the number of stripes or segments is increased accordingly. However, this applies only if all other parameters are kept constant. Interestingly, by proper regulation of the diffusion coefficient, our numerical simulations in the Turing regime confirm that it is possible to make the wavelength proportional to the system size and keep the number of stripes or segments invariant. Results of these simulations are shown in Fig. 12. For parameters η and τ in the Turing regime, we choose $\eta = 2.014$ and $\tau = 2.733$ and consider two systems with a scaling factor $\lambda = 2$. The spatial density distribution obtained from the simulations is shown in Figs. 12(a) and 12(b) for the two systems, respectively. Not unexpectedly, the patterns exhibit the same structure with equal number of stripes and segments. To further support

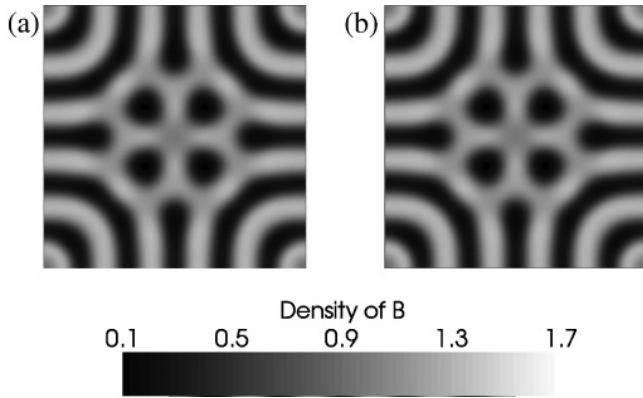


FIG. 12. Turing pattern showing spatial distribution of the density \tilde{B}^- at time $t = 400\,000$, $\eta = 2.016\,933$, and $\tau = 2.730\,30$ for two systems of size (a) 200×200 lattice units, (b) 400×400 lattice units. The patterns are clearly identical in the two cases.

this observation, we carried out numerical simulations over a range of system sizes from 50 to 500 lattice units. The thus-obtained density profiles along the line $y/L = 0.85$ are plotted in Fig. 13(a) for all studied system sizes. For the sake of visibility, each individual curve is shifted by a multiple of 2 along the vertical axis. It is clear from the figure that the number of stripes does not change with the system size. To further emphasize the similarity of the patterns, we directly compare in the same figure all the data using the same shift for all the curves. Clearly, the data collapse into a single curve.

As an additional demonstration of wavelength regulation and proportion preservation of the patterns, we perform Fourier transform of the patterns obtained from each system size in the range of 50 to 500 lattice units. We calculate the maximum excited wave number q_{\max} in the Fourier spectra of the density field using Eq. (44). Figure 13(b) shows the plot of the wave number excited with the system size for different diffusion coefficients. It is clear from the plot that the maximum excited wave number q_{\max} decreases in proportion to L and thus the generated pattern is expected to preserve the proportion as observed in our numerical simulation.

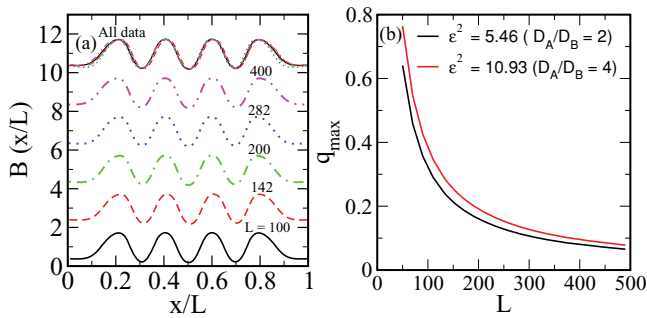


FIG. 13. (Color online) (a) Density profile of \tilde{B}^- along the line $y/L = 0.85$, obtained from the Turing pattern in Fig. 12 at time $t = 400\,000$, with parameters $\eta = 2.014$ and $\tau = 2.733$. The number of stripes are invariant over an appreciable range of system size. (b) Characteristic wave number of the Turing pattern in Fig. 12 plotted against the system size for different values of ϵ^2 (realized via a variation of D_A/D_B). The curve shows preservation of proportionality between the wave number and the system size.

V. SUMMARY

In this work, we study reaction-diffusion systems via lattice Boltzmann computer simulations. Starting from the analytical solution of a simple prototypical model (a single species undergoing transformation reaction and diffusion), we perform a systematic study of the lattice Boltzmann truncation error of the model. We uncover interesting behavior of the truncation error with the system parameters. The error is found to have a minimum at a given value of diffusion coefficient. The position of minimum is shifted for increasing values of the reaction rate constant. These observations are in agreement with the analytical findings from a third-order Chapman-Enskog multiscale expansion.

A study of the Gray-Scott reaction-diffusion model is also provided. Here, we perform a linear stability analysis of the model and determine the relevant parameter range for pattern formation. Lattice Boltzmann simulations of this interesting reaction-diffusion system are found to be in good agreement with the predictions of the linear stability analysis. In addition to a test of the linear stability phase diagram, lattice Boltzmann simulations provide valuable information on the details of the patterns formed in different regions of the parameter space. An example is the formation of striped patterns in most parts of the Turing regime above the Hopf bifurcation curve. Another very interesting example is provided by the so-called self-replicating spots, which lie beyond the linear stability regime. Self-replicating spots occur via large amplitude perturbations of the trivial homogeneous solution.

Furthermore, a survey of the parameters entering the scale invariant form of the Gray-Scott model suggests that the simplest choice to tune the length scale of the obtained patterns (while keeping its shape unchanged) is to multiply all the relevant diffusion coefficients with the same constant factor without any modification of the reaction rates. Interestingly, this leaves the time scale of the process unaffected. In other words, in systems with different diffusion coefficients but the same reaction rates, patterns exhibit the same shape (but different sizes) exactly for the same physical time. Results obtained via lattice Boltzmann simulations confirm this behavior. It is noteworthy that this act of regulating diffusion coefficient of species or morphogens, as the case may be, is also observed in some biological systems. This observation is by no means limited to this model—the analysis can also be extended to other reaction-diffusion models.

ACKNOWLEDGMENTS

This work was supported by the Max-Planck Initiative for Multiscale Materials Modeling of Condensed Matter (MMM) and the Interdisciplinary Center for Advanced Material Simulation (ICAMS). We are most grateful to Timm Krüger for useful discussions.

APPENDIX: CHAPMAN-ENSKOG PROCEDURE FOR REACTION-DIFFUSION EQUATION

In this appendix, we derive the macroscopic reaction-diffusion equation from the lattice Boltzmann model. The LB

equation for the reaction-diffusion equation is written as

$$f_{i,s}(\mathbf{x} + \mathbf{e}_i \Delta t, \Delta t + t) - f_{i,s}(\mathbf{x}, t) = \frac{f_{i,s}^{\text{eq}}(\mathbf{x}, t) - f_{i,s}(\mathbf{x}, t)}{\tau_s} + \Delta t w_i R_s. \quad (\text{A1})$$

To obtain a corresponding macroscopic partial differential equation from the finite difference Eq. (A1), we perform a Taylor series expansion of the left hand side of Eq. (A1) and obtain

$$\sum_{n=1}^{\infty} \frac{\Delta t^n}{n!} (\partial_t + e_{i\alpha} \partial_{x_\alpha})^n f_i(\mathbf{x}, t) = \frac{f_{i,s}^{\text{eq}}(\mathbf{x}, t) - f_{i,s}(\mathbf{x}, t)}{\tau_s} + \Delta t w_i R_s. \quad (\text{A2})$$

The Chapman Enskog procedure introduces two time scales, a fast time scale t_1 , associated with convective transport, and a slow time scale t_2 , associated with diffusion. The time derivative is then expanded as

$$\partial_t = \epsilon \partial_t^{(1)} + \epsilon^2 \partial_t^{(2)}. \quad (\text{A3})$$

The spatial derivative is written as

$$\partial_{x_\alpha} = \epsilon \partial_{x_\alpha}^{(1)}. \quad (\text{A4})$$

The equilibrium distribution as a reaction term is expanded as

$$f_{i,s} = f_{i,s}^{(0)} + \epsilon f_{i,s}^{(1)} + \epsilon^2 f_{i,s}^{(2)} + \epsilon^3 f_{i,s}^{(3)} + \mathcal{O}(\epsilon^4), \quad (\text{A5})$$

$$R_s = R_s^{(0)} + \epsilon R_s^{(1)} + \epsilon^2 R_s^{(2)} + \epsilon^3 R_s^{(3)} + \mathcal{O}(\epsilon^4). \quad (\text{A6})$$

Inserting Eqs. (A6), (A5), (A4), and (A3) in Eq. (A2), one obtains

$$\left[\Delta t (\epsilon \partial_t^{(1)} + \epsilon^2 \partial_t^{(2)} + \epsilon e_{i\alpha} \partial_{x_\alpha}^{(1)}) + \frac{\Delta t^2}{2} (\epsilon^2 \partial_t^{(1)} \partial_t^{(1)} + 2\epsilon^2 e_{i\alpha} \partial_t^{(1)} \partial_{x_\alpha}^{(1)} + \epsilon^2 e_{i\alpha} e_{i\beta} \partial_{x_\alpha}^{(1)} \partial_{x_\beta}^{(1)} + 2\epsilon^3 e_{i\alpha} \partial_t^{(2)} \partial_{x_\alpha}^{(1)} + 2\epsilon^3 \partial_t^{(2)} \partial_t^{(1)} + 2\epsilon^4 \partial_t^{(2)} \partial_t^{(2)}) \right] \times [f_{i,s}^{(0)} + \epsilon f_{i,s}^{(1)} + \epsilon^2 f_{i,s}^{(2)} + \mathcal{O}(\epsilon^3)] = \frac{1}{\tau_s} (f_{i,s}^{\text{eq}}(\mathbf{x}, t) - [f_{i,s}^{(0)} + \epsilon f_{i,s}^{(1)} + \epsilon^2 f_{i,s}^{(2)} + \epsilon^3 f_{i,s}^{(3)} + \mathcal{O}(\epsilon^4)]) + \Delta t w_i [\epsilon R_s^{(1)} + \epsilon^2 R_s^{(2)} + \epsilon^3 R_s^{(3)} + \mathcal{O}(\epsilon^4)]. \quad (\text{A7})$$

Grouping terms of the same order in ϵ yields the following successive approximations:

$$O(\epsilon^0) : f_{i,s}^{(0)} = f_{i,s}^{\text{eq}}, \quad \text{implying that} \quad R_s^{(0)} = 0. \quad (\text{A8})$$

Note that this condition follows directly from the conservation of mass.

$$O(\epsilon^1) : \Delta t (\partial_t^{(1)} + e_{i\alpha} \partial_{x_\alpha}^{(1)}) f_{i,s}^{(0)} = -\frac{1}{\tau_s} f_{i,s}^{(1)} + \Delta t w_i R_s^{(1)}. \quad (\text{A9})$$

On the level of ϵ , there is no mass diffusion; the diffusion process takes place on the scale of ϵ^2 . Furthermore, for diffusion driven reactions, the diffusive flux must bring the species together before the reaction and the reaction becomes a second-order effect. Since on the scale of ϵ , there is no mass diffusion, that implies $R_s^{(1)} = 0$. We would consider this case in this derivation and Eq. (A9) becomes

$$O(\epsilon^1) : \Delta t (\partial_t^{(1)} + e_{i\alpha} \partial_{x_\alpha}^{(1)}) f_{i,s}^{(0)} = -\frac{1}{\tau_s} f_{i,s}^{(1)}. \quad (\text{A10})$$

$$O(\epsilon^2) : \Delta t [\partial_t^{(2)} f_{i,s}^{(0)} + (\partial_t^{(1)} + e_{i\alpha} \partial_{x_\alpha}^{(1)}) f_{i,s}^{(1)}] + \frac{\Delta t^2}{2} (\partial_t^{(1)2} + 2e_{i\alpha} \partial_t^{(1)} \partial_{x_\alpha}^{(1)} + e_{i\alpha} e_{i\beta} \partial_{x_\alpha}^{(1)} \partial_{x_\beta}^{(1)}) \times f_{i,s}^{(0)} = -\frac{1}{\tau_s} f_{i,s}^{(2)} + \Delta t w_i R_s^{(2)}. \quad (\text{A11})$$

$$O(\epsilon^3) : \Delta t [\partial_t^{(3)} f_{i,s}^{(0)} + \partial_t^{(2)} f_{i,s}^{(1)} + (\partial_t^{(1)} + e_{i\alpha} \partial_{x_\alpha}^{(1)}) f_{i,s}^{(2)}] + \frac{\Delta t^2}{2} (\partial_t^{(1)2} + 2e_{i\alpha} \partial_t^{(1)} \partial_{x_\alpha}^{(1)} + e_{i\alpha} e_{i\beta} \partial_{x_\alpha}^{(1)} \partial_{x_\beta}^{(1)}) f_{i,s}^{(1)}$$

$$+ \Delta t^2 \partial_t^{(2)} (\partial_t^{(1)} + e_{i\alpha} \partial_{x_\alpha}^{(1)}) f_{i,s}^{(0)} + \frac{\Delta t^3}{6} (\partial_t^{(1)} + e_{i\alpha} \partial_{x_\alpha}^{(1)})^3 \times f_{i,s}^{(0)} = -\frac{1}{\tau_s} f_{i,s}^{(3)} + \Delta t w_i R_s^{(3)}. \quad (\text{A12})$$

Putting the expression for $f_{i,s}^{(1)}$ from Eq. (A10) into Eq. (A11) yields

$$\frac{1}{\tau_s} f_{i,s}^{(2)} = -\Delta t \partial_t^{(2)} f_{i,s}^{(0)} + \Delta t^2 \left(\tau_s - \frac{1}{2} \right) (\partial_t^{(1)} + e_{i\alpha} \partial_{x_\alpha}^{(1)})^2 \times f_{i,s}^{(0)} + \Delta t w_i R_s^{(2)}. \quad (\text{A13})$$

In Eq. (A12), we insert the expression for $f_{i,s}^{(1)}$ and $f_{i,s}^{(2)}$ from Eqs. (A10) and (A11) and obtain

$$\frac{1}{\tau_s} f_{i,s}^{(3)} = -\Delta t \partial_t^{(3)} f_{i,s}^{(0)} + \Delta t^2 (2\tau_s - 1) (\partial_t^{(1)} + e_{i\alpha} \partial_{x_\alpha}^{(1)}) \partial_t^{(2)} f_{i,s}^{(0)} - \Delta t^3 \left(\tau_s^2 - \tau_s + \frac{1}{6} \right) (\partial_t^{(1)} + e_{i\alpha} \partial_{x_\alpha}^{(1)})^3 \times f_{i,s}^{(0)} - \tau_s \Delta t^2 (\partial_t^{(1)} + e_{i\alpha} \partial_{x_\alpha}^{(1)}) w_i R_s^{(2)} + \Delta t w_i R_s^{(3)}. \quad (\text{A14})$$

Next we take the moments of the distribution functions in Eqs. (A9), (A13), and (A14). Note that in order to preserve the isotropy of the lattice tensors, the chosen lattice speeds and weights in the equilibrium distribution function must obey the

following moments or symmetry conditions:

$$\begin{aligned}
 (a) \sum_i w_i &= 1, & (b) \sum_i w_i e_{i\alpha} &= 0, \\
 (c) \sum_i w_i e_{i\alpha} e_{i\beta} &= c_s^2 \delta_{\alpha\beta}, & (d) \sum_i w_i e_{i\alpha} e_{i\beta} e_{i\gamma} &= 0, \\
 (e) \sum_i w_i e_{i\alpha} e_{i\beta} e_{i\gamma} e_{i\delta} &= c_s^4 (\delta_{\alpha\beta} \delta_{\gamma\delta} + \delta_{\alpha\gamma} \delta_{\beta\delta} + \delta_{\alpha\delta} \delta_{\beta\gamma}).
 \end{aligned} \quad (\text{A15})$$

Using Eq. (A15) and given that the local equilibrium takes the form $f_i^{\text{eq}} = f_i^{(0)} = w_i \rho_s$, we impose the following conditions of conservation of mass on the equilibrium distribution function,

$$\sum_i f_{i,s}^{(0)} = \rho_s, \quad \sum_i e_{i\alpha} f_{i,s}^{(0)} = 0, \quad \sum_i e_{i\alpha} e_{i\beta} f_{i,s}^{(0)} = \rho_s c_s^2 \delta_{\alpha\beta}. \quad (\text{A16})$$

We further assume that higher order corrections of the equilibrium distribution do not contribute to the local values of the mass, whereby obtaining

$$\sum_i f_i^{(n)} = 0 \quad \text{for } n \geq 1. \quad (\text{A17})$$

Taking \sum_i of Eq. (A9) and using Eqs. (A15), (A16), and (A17) yields

$$\partial_t^{(1)} \rho_s = 0. \quad (\text{A18})$$

Taking \sum_i Eq. (A13) and using Eqs. (A15), (A16), (A17), and (A18) leads to

$$\partial_t^{(2)} \rho_s = \Delta t c_s^2 (\tau_s - \frac{1}{2}) \partial_{x_\alpha}^{(1)} \partial_{x_\beta}^{(1)} \rho_s \delta_{\alpha\beta} + R_s^{(2)}. \quad (\text{A19})$$

Taking \sum_i of Eq. (A14) and using Eqs. (A15), (A16), (A17), and (A18) leads to

$$\begin{aligned}
 \partial_t^{(3)} \rho_s &= -3c_s^2 \Delta t^2 (\tau_s^2 - \tau_s + \frac{1}{6}) \partial_t^{(1)} \partial_{x_\alpha}^{(1)} \partial_{x_\beta}^{(1)} \rho_s \delta_{\alpha\beta} \\
 &\quad - \tau_s \Delta t^2 \partial_t^{(1)} R_s^{(2)} + R_s^{(3)}.
 \end{aligned} \quad (\text{A20})$$

We multiply Eq. (A18) by ϵ , Eq. (A19) by ϵ^2 , and Eq. (A20) by ϵ^3 and add all this together, thus arriving at

$$\begin{aligned}
 \partial_t \rho_s &= c_s^2 \Delta t (\tau_s - \frac{1}{2}) \partial_{x_\alpha}^2 \rho_s + R_s - 3\Delta t^2 c_s^2 \\
 &\quad \times (\tau_s^2 - \tau_s + \frac{1}{6}) \partial_t \partial_{x_\alpha}^2 \rho_s - \tau_s \Delta t^2 \partial_t R_s.
 \end{aligned} \quad (\text{A21})$$

We can further re-write Eq. (A21) as the macroscopic reaction-diffusion equation and a third-order truncation error term E ,

$$\partial_t \rho_s = D_s \partial_{x_\alpha}^2 \rho_s + R_s - E, \quad (\text{A22})$$

where the diffusion coefficient is given by $D_s = c_s^2 \Delta t (\tau_s - 0.5)$ and the error term takes the form

$$E = 3\Delta t^2 c_s^2 (\tau_s^2 - \tau_s + \frac{1}{6}) \partial_t \partial_{x_\alpha}^2 \rho_s + \tau_s \Delta t^2 \partial_t R_s + \mathcal{O}(\epsilon^4). \quad (\text{A23})$$

-
- [1] F. T. Arecchi, S. Boccaletti, and P. Ramazza, *Phys. Rep.* **318**, 1 (1999).
- [2] R. E. Wilson, *Philos. Trans. R. Soc. London, Ser. A* **366**, 2017 (2008).
- [3] I. R. Epstein and K. Showalter, *J. Phys. Chem.* **100**, 13132 (1996).
- [4] A. De Wit, *Adv. Chem. Phys.* **109**, 435 (1999).
- [5] F. Sagués and I. R. Epstein, *Dalton Trans.* **7**, 1201 (2003).
- [6] J. D. Murray, *Mathematical Biology I: An Introduction* (Springer-Verlag, Berlin, 2002).
- [7] J. D. Murray, *Mathematical Biology II: Spatial Models and Biomedical Applications* (Springer-Verlag, Berlin, 2003).
- [8] I. R. Epstein, *Proc. Natl. Acad. Sci. USA* **103**, 15727 (2006).
- [9] S. Kitsunzaki, *Physica D* **216**, 294 (2006).
- [10] A. A. Polezhaev, R. A. Pashkov, A. I. Lobanov, and I. B. Petrov, *Int. J. Dev. Biol.* **50**, 309 (2006).
- [11] S. J. Schiff, X. Huang, and J.-Y. Wu, *Phys. Rev. Lett.* **98**, 178102 (2007).
- [12] K. Agladze, E. Dulos, and P. De Kepper, *J. Phys. Chem.* **96**, 2400 (1992).
- [13] A. M. Turing, *Philos. Trans. R. Soc. London* **237** (1952).
- [14] G. Nicolis and I. Prigogine, *Self-Organization in Nonequilibrium Systems: From Dissipative Structures to Order through Fluctuations* (Wiley, New York, 1977).
- [15] J. Tabony, N. Glade, J. Demongeot, and C. Papaseit, *Langmuir* **18**, 7196 (2002).
- [16] J. Huang, D. A. Vasquez, B. F. Edwards, and P. Kolodner, *Phys. Rev. E* **48**, 4378 (1993).
- [17] S. Ruuth, *J. Math. Biol.* **34**, 148 (1995).
- [18] J. Martin, N. Rakotomalala, D. Salin, and M. Böckmann, *Phys. Rev. E* **65**, 051605 (2002).
- [19] A. Kassam and L. N. Trefethen, *SIAM J. Sci. Comput.* **26**, 1214 (2005).
- [20] A. Madzvamuse, *J. Comput. Phys.* **214**, 239 (2006).
- [21] W. H. Hundsdorfer and J. G. Verwer, *Numerical Solution of Time Dependent Advection Diffusion Reaction Equations*, Springer Series in Computational Mathematics No. 33 (Springer-Verlag, Berlin, 2003).
- [22] L. Sebestikova, J. D'Hernoncourt, M. J. B. Hauser, S. C. Müller, and A. De Wit, *Phys. Rev. E* **75**, 026309 (2007).
- [23] F. Varnik, D. Dorner, and D. Raabe, *J. Fluid Mech.* **573**, 191 (2007).
- [24] F. Varnik and D. Raabe, *Modell. Simul. Mater. Sci. Eng.* **14**, 857 (2006).
- [25] S. Succi, R. Benzi, and F. Higuera, *Physica D* **47**, 219 (1991).
- [26] D. Rothman, *J. Geophys. Res.* **95**, 8663 (1990).
- [27] D. Rothman and J. M. Keller, *J. Stat. Phys.* **52**, 1119 (1988).
- [28] T. Ishikawa, *J. R. Soc. Interface* **6**, 815 (2009).
- [29] C. M. Pooley and J. M. Yeomans, *Comput. Phys. Commun.* **179**, 159 (2008).
- [30] A. Smith, V. Nikora, A. Ross, and G. Wake, *Ecol. Modell.* **192**, 645 (2006).
- [31] Q. Kang, D. Zhang, S. Chen, and X. He, *Phys. Rev. E* **65**, 036318 (2002).
- [32] S. P. Dawson, S. Chen, and G. D. Doolen, *J. Chem. Phys.* **98**, 15 (1993).

- [33] R. Blaak and P. M. A. Sloot, *Comput. Phys. Commun.* **129**, 256 (2000).
- [34] J. E. Pearson, *Science* **261**, 189 (1993).
- [35] K. J. Lee, W. D. McCormick, J. E. Pearson, and H. L. Swinney, *Nature (London)* **369**, 215 (1994).
- [36] C. B. Muratov and V. V. Osipov, *Phys. Rev. E* **60**, 242 (1999).
- [37] A. Doelman, T. J. Kaper, and P. A. Zegeling, *Nonlinearity* **10**, 523 (1997).
- [38] Y. Nishiura and D. Ueyama, *Physica D* **150**, 137 (2001).
- [39] W. N. Reynolds, J. E. Pearson, and S. Ponce-Dawson, *Phys. Rev. Lett.* **72**, 2797 (1994).
- [40] S. Kondo and R. Asai, *Nature (London)* **376**, 765 (2002).
- [41] B. Houchmandzadeh, E. Wieschais, and S. Leibler, *Nature (London)* **415**, 798 (2002).
- [42] K. Kaneko and T. Yomo, *Physica D* **75**, 89 (1994).
- [43] T. Mizuguchi and M. Sano, *Phys. Rev. Lett.* **75**, 966 (1995).
- [44] H. G. Othmer and E. Pate, *Proc. Natl. Acad. Sci. USA* **77**, 4180 (1980).
- [45] E. Pate and H. G. Othmer, *Differentiation* **28**, 1 (1984).
- [46] A. Hunding and P. G. Srensen, *J. Math. Biol.* **26**, 27 (1988).
- [47] T. Aegerter-Wilmsen, C. M. Aegerter, and T. Bisseling, *J. Theor. Biol.* **234**, 13 (2005).
- [48] S. Ishihara and K. Kaneko, *J. Theor. Biol.* **238**, 683 (2006).
- [49] G. R. McNamara and G. Zanetti, *Phys. Rev. Lett.* **61**, 2332 (1988).
- [50] F. Higuera, S. Succi, and R. Benzi, *Europhys. Lett.* **9**, 345 (1989).
- [51] Y. Qian, D. d’Humières, and P. Lallemand, *Europhys. Lett.* **17**, 479 (1992).
- [52] S. Succi, *The Lattice-Boltzmann Equation: For Fluid Dynamics and Beyond* (Clarendon Press, Oxford, 2001).
- [53] R. Rubinstein and L. S. Luo, *Phys. Rev. E* **77**, 036709 (2008).
- [54] U. Frisch, D. d’Humières, B. Hasslacher, P. Lallemand, Y. Pomeau, and J.-P. Rivet, *Complex Syst.* **1**, 649 (1987).
- [55] S. Arcidiacono, I. V. Karlin, J. Mantzaras, and C. E. Frouzakis, *Phys. Rev. E* **76**, 046703 (2007).
- [56] S. Arcidiacono, J. Mantzaras, and I. V. Karlin, *Phys. Rev. E* **78**, 046711 (2008).
- [57] P. De Kepper, I. R. Epstein, K. Kustin, and M. Orban, *J. Phys. Chem.* **86**, 170 (1982).
- [58] I. Szalai and P. De Kepper, *J. Phys. Chem. A* **108**, 5315 (2004).
- [59] S. G. Ayodele, F. Varnik, and D. Raabe, *Phys. Rev. E* **80**, 016304 (2009).
- [60] M. R. Wang and Q. J. Kang, *J. Comput. Phys.* **229**, 728 (2010).
- [61] T. Krüger, F. Varnik, and D. Raabe, *Phys. Rev. E* **79**, 046704 (2009).